

SURFACE LAYER ACCRETION IN TRANSITIONAL AND CONVENTIONAL DISKS: FROM POLYCYCLIC AROMATIC HYDROCARBONS TO PLANETS

DANIEL PEREZ-BECKER

Department of Physics, University of California, Berkeley, CA 94720, USA

AND

EUGENE CHIANG

Departments of Astronomy and Earth and Planetary Science, University of California, Berkeley, CA 94720, USA

Draft version September 25, 2018

ABSTRACT

“Transitional” T Tauri disks have optically thin holes with radii $\gtrsim 10$ AU, yet accrete up to the median T Tauri rate. Multiple planets inside the hole can torque the gas to high radial speeds over large distances, reducing the local surface density while maintaining accretion. Thus multi-planet systems, together with reductions in disk opacity due to grain growth, can explain how holes can be simultaneously transparent and accreting. There remains the problem of how outer disk gas diffuses into the hole. Here it has been proposed that the magnetorotational instability (MRI) erodes disk surface layers ionized by stellar X-rays. In contrast to previous work, we find that the extent to which surface layers are MRI-active is limited not by ohmic dissipation but by ambipolar diffusion, the latter measured by Am : the number of times a neutral hydrogen molecule collides with ions in a dynamical time. Simulations by Hawley & Stone showed that $Am \sim 100$ is necessary for ions to drive MRI turbulence in neutral gas. We calculate that in X-ray-irradiated surface layers, Am typically varies from $\sim 10^{-3}$ to 1, depending on the abundance of charge-adsorbing polycyclic aromatic hydrocarbons, whose properties we infer from *Spitzer* observations. We conclude that ionization of H_2 by X-rays and cosmic rays can sustain, at most, only weak MRI turbulence in surface layers 1–10 g/cm² thick, and that accretion rates in such layers are too small compared to observed accretion rates for the majority of disks.

Subject headings: accretion, accretion disks — instabilities — ISM: molecules — MHD — planetary systems: protoplanetary disks — stars: pre-main sequence

1. INTRODUCTION

On the road from molecular clouds to planetary systems, transitional disks are among the brightest signposts. Encircling T Tauri and Herbig Ae/Be stars having ages of 1–10 Myr, these disks have large inner holes nearly devoid of dust. Identified by spectral energy distributions (SEDs; e.g., Strom et al. 1993; Calvet et al. 2005; Kim et al. 2009) and imaged directly (e.g., Ratzka et al. 2007; Hughes et al. 2007; Brown et al. 2009), transitional disk cavities have radii on the order of 3–100 AU. Transitional disks are so named (Strom et al. 1990) because they might represent an evolutionary link between optically thick disks without holes (e.g., Watson et al. 2007) and debris disks containing only rings of optically thin dust (e.g., Wyatt 2008). They are of special interest not least because their central clearings may harbor nascent planets, potentially detectable against relatively weak backgrounds.

1.1. *The Need for Companions*

The idea that transitional disk holes are swept clean by companions, possibly of planetary mass, is natural. We adhere to this interpretation, although not all our arguments as given below are the ones usually discussed.

1.1.1. *Stellar-mass Companions*

Roughly half of all transitional disks—6 out of 13 in the sample of Kim et al. (2009)—are already known to

contain stellar-mass companions. A prototypical example is CoKu Tau/4: a transitional system whose hole is practically empty, both of dust (D’Alessio et al. 2005) and gas (G. Blake, private communication, 2007). Inside its hole of radius ~ 10 AU resides a nearly equal mass K-star binary having a projected separation of 8 AU (Ireland & Kraus 2008). Gravitational torques exerted by the binary can easily counteract viscous torques in the disk (Goldreich & Tremaine 1980), staving off accretion onto either star (Artymowicz & Lubow 1994; Ochi et al. 2005). Indeed stellar accretion rates for CoKu Tau/4 are unmeasurably small, $\lesssim 10^{-10} M_\odot \text{ yr}^{-1}$ (Najita et al. 2007).

Not every hole, however, is as empty as that of CoKu Tau/4. In many cases there is a sprinkling of dust: optical depths at 10 μm wavelength for many sources range from 0.01–0.1 (Calvet et al. 2002, 2005). Observations of rovibrational emission from warm, optically thick CO imply that gas fills many disk holes (Salyk et al. 2007), albeit with surface densities that may be far below those of conventional disks (we will argue below that this is in fact the case). Most germane to our work, the host stars of many transitional systems actively accrete, at rates that on average are somewhat lower than those of conventional disks (Najita et al. 2007), but which in several instances approach $10^{-8} M_\odot \text{ yr}^{-1}$, the median T Tauri rate. The holes of these systems must contain accreting gas.

How can we reconcile the fact that many holes contain

Electronic address: perez-becker@berkeley.edu

gas, accreting at rates approaching those of conventional disks, with the fact that the holes contain only trace amounts of dust? To explain the paradox of simultaneous accretion and hole transparency, appeals are sometimes made to grain growth, or the filtering of dust out of gas by hydrodynamic mechanisms (Paardekooper & Mellema 2006; Rice et al. 2006) or radiation pressure (Chiang & Murray-Clay 2007).

These proposals, which invoke changes in disk opacity, may be part of the solution. But they cannot alone explain the observations. Ward (2009) has criticized the hydrodynamic filter. The force of radiation pressure depends on uncertain optical constants and grain porosities, and is likely to expel only grains having a narrow range of sizes (Burns et al. 1979). Even if grains have the right properties to be blown out by radiation pressure in vacuum, the inward flow of accreting gas may be strong enough to carry as much as half of the grains that leak from the rim into the hole (Chiang & Murray-Clay 2007). Grain growth does not explain why transitional disk accretion rates \dot{M} tend to be several times smaller than for conventional T Tauri systems (Najita et al. 2007). Finally, none of these proposals predicts gapped (“pre-transitional”) disks, which are optically thick at stellocentric distances $a \lesssim 0.15$ AU (e.g., LkCa 15; Espaillat et al. 2007a).

An alternative explanation for why holes can be simultaneously transparent and still contain accreting gas involves the special way in which disk gas accretes in the presence of companions, particularly those on eccentric orbits. If the hole rim leaks gas—and for some combinations of disk viscosity, disk pressure, and binary parameters the rim can be quite leaky (Artymowicz & Lubow 1996; Ochi et al. 2005)—the gas can suddenly plunge inward at rates approaching freefall velocities. The catastrophic loss of angular momentum is enabled by the non-axisymmetric and time-dependent potential of the eccentric binary, which directs gas streamlines onto radial orbits that may intersect and shock. Artymowicz & Lubow (1996) explained the paradox of simultaneous accretion and transparency:

“... [for some circumbinary disk parameters] gravitational resonant torques are able to open a fairly wide gap [hole], while *concurrently* the accretion flow proceeds through that gap in the form of time-dependent, *well-developed* or *efficient* gas stream(s) carrying virtually all the unimpeded mass flux. The radial velocity of the stream is of order [the Kepler velocity], i.e., $\sim Re$ [Reynolds number] times faster than in the disk. By mass conservation, the axially averaged surface density must differ by a factor of $Re > 10^3$ between the gap and the disk edge region. ... The spectroscopic ramification of this is a deficit of the observed radiation flux emitted at temperatures appropriate for the gap location.” (italics theirs)

Thus reductions in the dust-to-gas ratio by grain growth or dust filtration are not the only processes that can render accreting gas transparent in transitional disk holes. Companions can accelerate disk gas to such high

radial speeds that, by mass continuity, the surface density in *both* gas and dust is reduced by orders of magnitude. According to this explanation, the reduction in total surface density is not necessarily due to consumption of gas by companions, but is rather due to gravitational forcing.

1.1.2. Multiple Planetary Mass Companions

Though a stellar-mass companion can exert torques strong enough to maintain holes of large size, a single planet-mass companion on a circular orbit cannot do the same job. For observationally reasonable values of the disk viscosity, a single companion having of order ~ 1 Jupiter mass embedded within a disk at least a few times more massive carves out only a narrow gap (e.g., Lubow & D’Angelo 2006; Crida & Morbidelli 2007). Disk gas funnels past the planet by traveling on horseshoe-like orbits (Lubow et al. 1999). A single planet may siphon off some of the gas that flows past it, but the disk accretion rate inside the planet’s orbit is reduced from that outside by a factor of $\lesssim 10$ (Lubow & D’Angelo 2006). This modest reduction in \dot{M} , combined with the narrowness of the gap seen in simulations ($\Delta r/r \sim 0.1$), implies inner disks far too extensive and optically thick to explain transitional systems.

How, then, do planets fit in? In those cases where the central stars of transitional disks lack stellar-mass companions, the same tasks of maintaining hole rims and increasing accretion velocities v (but not accretion rates \dot{M}) can be performed, not by a single planet, but by a system of multiple planets. We imagine a series of planets, with the outermost lying just interior to and shepherding the hole rim. Gas that leaks from the rim is torqued from planet to planet, all the way down to the central star, its optical depth decreasing inversely as its radial speed. The more massive the planets and the more eccentric their orbits, the fewer of them should be required.

Such a picture is supported by numerical simulations of Jupiter and Saturn embedded within a viscous disk (Masset & Snellgrove 2001; Morbidelli & Crida 2007). In these simulations the two planets were close enough that their gaps overlapped. Gas outside Saturn’s orbit executed half a horseshoe turn relative to Saturn, and then another half-horseshoe turn relative to Jupiter, thereby crossing from the outer disk through the Jupiter-Saturn common gap into the inner disk. Morbidelli & Crida (2007) found that the surface density in the gap region was reduced by 1–2 orders of magnitude, at least near Jupiter.

As our paper was being reviewed, we became aware of planet-disk simulations by Zhu et al. (2010, submitted) which included as many as 4 Jupiter-mass planets and whose results supported those of Morbidelli & Crida (2007). Depending on the assumed efficiency with which planets consumed disk gas, a set of four planets was found to reduce surface densities in their vicinity by up to 2 orders of magnitude, while disk accretion rates were reduced by factors $\lesssim 10$ (see their run P4A10). However, such surface density suppressions are not by themselves large enough to explain the observed low optical depths of disk holes. Zhu et al. (2010) concluded that reductions in gas opacity by some means of dust depletion

(e.g., grain growth) are still required.

Companions can also accommodate gapped or “pre-transitional” disks in which optically thin holes contain optically thick annuli. As inferred from spatially unresolved spectra, these annuli are narrow and about their host stars, extending mere fractions of an AU in radius (Espaillat et al. 2007a; but see also Eisner et al. 2009 who showed using spatially resolved observations that the gapped disk interpretation of SR 21 is incorrect). In regions far removed from secondary companions—in particular, in those regions closest to the primary star where the potential is practically that of a point mass—the in-fall speeds of accreting gas must slow back down to the normal rate set by disk viscosity. By continuity, the surface density must rise back up, and optical thickness is thus restored.

1.2. *Companions are Not Enough: The Case for the Magnetorotational Instability for the Origin of Disk Viscosity*

Our case for companions presumes a source of disk viscosity. While a stellar-mass companion or a system of multiple planets can transport gas quickly, effectively generating an enormous viscosity in their vicinity (i.e., inside the hole), they cannot cause the outer disk to diffuse in the first place. An inviscid outer disk will not leak. Another source of viscosity has to act in the outer disk, causing it bleed inward and supply the observed accretion rates \dot{M} . We now turn to the main subject of this paper, the possibility that the magnetorotational instability is the source of viscosity in the outer disk.

The magnetorotational instability (MRI) amplifies magnetic fields in outwardly shearing disks and drives turbulence whose Maxwell stresses transport angular momentum outward and mass inward (for a review, see Balbus 2009). Gas must be sufficiently well ionized for the MRI to operate. For the most part, T Tauri and Herbig Ae disks are too cold at their midplanes for thermal ionization to play a role there. The hope instead is that X-rays emitted by host stars can provide the requisite ionization in irradiated disk surface layers (Glassgold et al. 1997). The basic picture was conceived by Gammie (1996), who proposed that disk surface layers ionized by some non-thermal means may accrete, leaving behind magnetically “dead” midplane gas. Like other workers (e.g., Bai & Goodman 2009, hereafter BG; and Turner et al. 2010, hereafter TCS), we focus in this study on ionization of H₂ by X-rays. Ionization of trace species by ultraviolet (UV) radiation is also potentially important—we discuss this topic briefly at the close of our paper.

The exposed rim of a transitional disk constitutes a kind of surface layer. X-rays may penetrate the rim wall, activate the MRI there, and dislodge a certain radial column of gas every diffusion time (Chiang & Murray-Clay 2007, hereafter CMC). Within the MRI-active column, both the magnetic Reynolds number

$$Re \equiv \frac{c_s h}{D} \approx 1 \left(\frac{x_e}{10^{-13}} \right) \left(\frac{T}{100 \text{ K}} \right)^{1/2} \left(\frac{a}{\text{AU}} \right)^{3/2} \quad (1)$$

and the ion-neutral collision rate (normalized to the or-

bit frequency)

$$Am \equiv \frac{x_i n_{\text{H}_2} \beta_{\text{in}}}{\Omega} \approx 1 \left(\frac{x_i}{10^{-8}} \right) \left(\frac{n_{\text{H}_2}}{10^{10} \text{ cm}^{-3}} \right) \left(\frac{a}{\text{AU}} \right)^{3/2} \quad (2)$$

must be sufficiently large for magnetic fields to couple well to the overwhelmingly neutral disk gas. Here T is the gas temperature, c_s is the gas sound speed, $h = c_s/\Omega$ is the gas scale height, Ω is the Kepler orbital frequency, $D = 234(T/\text{K})^{1/2} x_e^{-1} \text{ cm}^2 \text{ s}^{-1}$ is the magnetic diffusivity, $x_{e(i)}$ is the fractional abundance of electrons (ions) by number, n_{H_2} is the number density of hydrogen molecules, $\beta_{\text{in}} \approx 1.9 \times 10^{-9} \text{ cm}^3 \text{ s}^{-1}$ is the collisional rate coefficient for ions to share their momentum with neutrals (Draine et al. 1983), and a is the disk radius.

Dimensionless number (1) governs how well magnetic fields couple to plasma, while (2) assesses how well plasma couples to neutral gas. Both these numbers must be large for good coupling between magnetic fields and neutral gas. Numerical simulations have suggested critical values Re^* of $\sim 10^2$ – 10^4 (Fleming et al. 2000),¹ depending on the initial field geometry, and Am^* of $\sim 10^2$ (Hawley & Stone 1998, hereafter HS). Some studies (e.g., TCS) assumed $Am^* \sim 1$ in their determination of the thicknesses of MRI-active surface layers, but numerical simulations of marginally coupled ion-neutral systems indicated Am^* may be 2 orders of magnitude higher (HS). The value of Am^* is critical to our work.

For typical T Tauri parameters, CMC found active radial column densities $N^* \sim 5 \times 10^{23} \text{ cm}^{-2}$ or equivalently mass columns of $\Sigma^* \sim 2 \text{ g cm}^{-2}$ —essentially the stopping column for 3 keV X-rays. When they combined their derived value for N^* with an assumed value for the dimensionless disk viscosity $\alpha \sim 10^{-2}$, the accretion rates of many transitional systems were successfully reproduced. According to this model, the maximum accretion rate \dot{M} inside the hole is set by conditions at the rim wall, i.e., by how large a radial column N^* the MRI can draw from the rim. Stellar or planetary companions, known or suspected to be present (Section 1.1), regulate how quickly this leaked material spirals onto the host star—these companions modulate the radial inflow speed $v(a)$ and thus the surface density $\Sigma(a) = \dot{M}/(2\pi va)$. But the companions inside the hole do not initiate disk accretion. They may reduce \dot{M} by exerting repulsive torques to keep material in the rim wall from leaking in, or by accreting material that flows past (e.g., Lubow & D’Angelo 2006; Najita et al. 2007). But they do not generate a non-zero \dot{M} in the first place. That fundamental task is left to the MRI operating at the rim—or whatever source of anomalous viscosity must be present in the outer disk to make it bleed.

¹ The magnetic Reynolds number as we define it is not as accurate a predictor of MRI turbulence as the Elsasser (a.k.a. Lundquist) number, which is given by (1) with c_s replaced by the vertical Alfvén speed v_{A_z} . Self-consistent resistive MHD simulations by Turner et al. (2007) found that MRI-active regions coincide with Elsasser numbers greater than unity (see also Sano & Inutsuka 2001; Sano & Stone 2002). Our criterion $Re \gtrsim 10^2$ – 10^4 offsets some of the inaccuracy because $v_{A_z} \lesssim 10^{-1} c_s$ in simulations of MRI turbulence. In any case we will find that the limiting factor for active surface layers is not Re but rather Am .

1.3. The Threat Posed by Polycyclic Aromatic Hydrocarbons to the MRI

One concern raised by CMC but left quantitatively unaddressed is the degree to which ultra-small condensates—macromolecules whose sizes are measured in angstroms—may thwart the MRI. In planetary atmospheres, aerosols can strongly damp electrical conductivities (e.g., Schunk & Nagy 2004; Borucki & Whitten 2008).² Most studies of active layers neglect aerosols and fixate on roughly micron-sized grains, despite the fact that in many particle size distributions, the smallest particles collectively present the greatest geometric surface area and therefore the greatest cross section for electron adsorption and ion recombination. Exceptions include Sano et al. (2000), who in one model considered a grain size distribution extending down to $0.005 \mu\text{m} = 50 \text{ \AA}$, and BG, who considered grain sizes as small as $0.01 \mu\text{m} = 100 \text{ \AA}$. Both studies found that in principle small grains can be deadly to the MRI.

Notwithstanding their possibly decisive role, small grains are sometimes wishfully dismissed as being depleted in number by grain growth, i.e., assimilated into larger grains. Undeniably grains grow (Blum & Wurm 2008; Chiang & Youdin 2010), so much so that their collective mass may be concentrated in particles millimeters in size. But the question relevant for ionization chemistry is not where the mass is weighted in the size spectrum of particles, but rather where the collective surface area for charge neutralization is weighted. Determining the grain size distribution in disks seems a problem that cannot be forward modeled with confidence. Sano et al. (2000) and BG instead parameterized the population of small grains and studied the effects of varying their numbers, leaving undecided the question of whether their parameter choices were favored by observation or theory.

Like Sano et al. (2000) and BG, this paper considers the effects of small condensates on the MRI. What is new about our contribution is that we consider the smallest imaginable condensates that are still accessible to observation: polycyclic aromatic hydrocarbons (PAHs). These molecules, typically containing several dozens of carbon atoms, are excited electronically by ultraviolet radiation and fluoresce vibrationally at 3.3, 6.2, 7.7, 8.6, 11.3, and $12.7 \mu\text{m}$, the signature bands of their constituent C-C and C-H bonds (e.g., Li & Draine 2001; Pendleton & Allamandola 2002). *Spitzer* satellite spectra and ground-based adaptive optics imaging reveal PAHs to be fluorescing strongly in Herbig Ae/Be and T Tauri disk surface layers directly exposed to stellar ultraviolet radiation (Geers et al. 2006, 2007; Goto et al. 2009). Thus PAHs help to constrain the aerosol abundance where magnetically driven accretion is thought to occur: in disk surface layers.

In this work we incorporate PAHs into a simple chemical network to assess the proposal that X-ray driven MRI operates in disk surface layers, either on the top and bottom faces of conventional hole-less disks, or at the rims of transitional disks. We make as realistic an estimate as

we can of the PAH abundance based on observations, to gauge how deep the X-ray-irradiated, MRI-active layer might actually be.

To summarize this introduction: companions—either stars or a system of multiple planets, but not a single Jupiter-mass planet—can help clear the extensive holes of transitional disks. The outermost companion serves to establish the location of the rim where viscous torques in the disk and gravitational torques from the companion seek balance. If gas leaks inward from the outer disk, it is driven onto the host star so quickly by gravitational torques from companions that its optical depth may be reduced by orders of magnitude. Companions, together with reductions in disk opacity by grain growth, thus maintain the transparency of the hole while still permitting stars to accrete gas. But companions do not, in and of themselves, cause gas in the outer disk to diffuse inward. That responsibility may be reserved for the MRI—whose ability to operate despite the presence of charge-neutralizing PAHs is the subject of this paper.

Our paper is organized as follows. The ingredients of our numerical model for X-ray-driven ionization chemistry in disk surface layers are laid out in Section 2. There we gauge what PAH abundances in disks may be. Results—principally, how Am and Re vary with the column density penetrated by X-rays, and the extent to which PAHs reduce these numbers—are presented in Section 3. Analytic interpretations of our numerical results, and direct comparison with previous calculations (BG, TCS), are given there as well. We discuss our main results for X-ray driven MRI in Section 4, and close by discussing the possibility of UV-driven MRI.

2. MODEL FOR DISK IONIZATION

In this paper we are interested in the degree to which stellar X-rays and Galactic cosmic-rays can ionize H_2 gas in T Tauri disks. In this respect our study is similar to many others, and we make direct comparisons of our work to BG and TCS in Section 3.4. For simplicity our model neglects ionization of trace species like C and S by stellar UV radiation. Omitting UV-driven chemistry renders our model inconsistent because our model also includes PAHs, whose abundances we constrain in Section 2.4.3 by using observed PAH emission lines excited by stellar UV radiation. We will discuss the critical issue of UV ionization in Section 4.1.

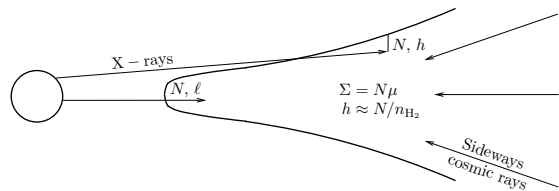


FIG. 1.— X-ray ionized surface layers, located either on the top and bottom faces of a flared disk, or at its inner rim. Our calculations apply to both situations, although they are more accurate for the former. We assume in this work that the lengthscale ℓ over which gas is distributed radially at the hole rim is equal to h , the vertical gas scale height. Other sources of ionization are interstellar cosmic-rays and ultraviolet radiation from the star. At large stellocentric distances ($a \gtrsim 30 \text{ AU}$), cosmic rays may penetrate the disk from the side. For most of our paper, we neglect ionization of trace species by far ultraviolet radiation, but in Section 4.1 we briefly discuss this important topic.

² Some fire alarms work on this principle. A radioactive source inside the alarm drives ionization currents in the air which normally complete an electrical circuit. When smoke particles from a fire reduce the density of free ions and electrons in air, the circuit is broken and the alarm is triggered.

2.1. X-ray and Cosmic-ray Ionization Rates and Gas Densities

Chandra spectra of pre-main-sequence stars in the Orion Nebula can be fitted by a pair of thermal plasmas with characteristic temperatures $kT_X \sim 1$ and 3 keV, where k is Boltzmann’s constant, and comparable luminosities $L_X \sim 10^{28}$ – 10^{31} erg s $^{-1}$ (Wolk et al. 2005; Preibisch et al. 2005). The softer component is believed to be emitted by shock-heated accreting gas (Stelzer & Schmitt 2004), and the harder component by a strongly magnetized and active stellar corona (Wolk et al. 2005). X-ray luminosities tend to increase with increasing stellar mass and decreasing accretion rate (see Figure 1 of Telleschi et al. 2007, and Figure 17 of Preibisch et al. 2005). These correlations are relevant for transitional disks because some transitional disks are hosted by higher mass Herbig Ae stars, and accretion rates for transitional disks tend to be lower than for conventional disks (Najita et al. 2007). For our standard model we will adopt $L_X = 10^{29}$ erg s $^{-1}$, but we will also experiment with $L_X = 10^{31}$ erg s $^{-1}$. We fix the temperature of the X-ray emitting plasma at $kT_X = 3$ keV, an assumption that ignores how X-ray spectra harden with increasing L_X (Preibisch et al. 2005). Although none of our numerical models explicitly considers $kT_X > 3$ keV, we will discuss quantitatively in Section 3.3.1 how our results scale with the higher ionization rates afforded by a harder ($kT_X = 8$ keV) X-ray spectrum; we will see there that the effects are not large.³ See Table 1 for a list of all model parameters.

We derive X-ray ionization rates ζ_X as a function of penetration column N from Igea & Glassgold (1999, hereafter IG), who constructed a Monte Carlo radiative transfer model that accounts for Compton scattering and photoionization. Compton scattering enables X-ray photons to penetrate to deeper columns than would otherwise be possible. For our standard model we use IG’s Figure 3 for a thermal plasma of $L_X = 10^{29}$ erg s $^{-1}$ and $kT_X = 3$ keV. Their ionization rates were computed for stellocentric distances of 5 and 10 AU; we scale these rates to the stellocentric distances of our model, $a = 3$ and 30 AU, using the geometric dilution factor a^{-2} . We test the accuracy of this approach by scaling their results internally using this dilution factor, finding (by necessity) excellent agreement at low columns where material is optically thin to X-rays, and agreement better than a factor of two at the highest columns calculated. For the case $L_X = 10^{31}$ erg s $^{-1}$, we increase all ionization rates from our standard values by a factor of 100.

Interstellar cosmic-rays can also ionize disk gas, but are attenuated by magnetized stellar winds blowing across disk surface layers. Even the contemporary solar wind, characterized by a mass loss rate of $\sim 10^{-14} M_\odot$ yr $^{-1}$, modulates the cosmic-ray flux at Earth by as much as $\sim 10\%$ with solar cycle (Marsh & Svensmark 2003). T Tauri winds, having mass loss rates up to 5 orders of

magnitude higher than that of the solar wind today, seem likely to shield disk surfaces from cosmic-rays directed normal to the disk plane (cf. Turner & Drake 2009). Nevertheless, cosmic-rays may reach disk gas from the “side,” striking the disk edge-on from the outside. At $a = 3$ AU we estimate that these “sideways cosmic-rays” are too strongly attenuated by intervening disk gas to be significant. The same is not true on the outskirts of the disk at $a = 30$ AU, where column densities measured radially outward may be smaller than the cosmic-ray stopping column of 96 g cm $^{-2}$ (Umebayashi & Nakano 1981). Thus we consider another model at $a = 30$ AU where in addition to our standard X-ray source we include sideways cosmic-rays with a constant, column-independent ionization rate of $\zeta_{CR} \sim (1/4) \times 10^{-17}$ s $^{-1}$ (Caselli et al. 1998, hereafter C98). The factor of 1/4 is approximately the fraction of the celestial sphere (centered on disk gas at 30 AU) that is not shielded by stellar winds. The total ionization rate $\zeta = \zeta_X + \zeta_{CR}$.

In all our simulations we neglect ionization by energetic protons emitted by the stars. As discussed by Turner & Drake (2009), estimates of the stellar proton flux rely on extrapolated scaling relations, and the ability of particles to reach the disk surface in the face of strong stellar magnetic fields is uncertain. Moreover, protons are emitted in flares which may occur too infrequently to sustain disk ionization. In one of their models, Turner & Drake (2009) used a time-steady stellar particle luminosity whose ionization rate exceeded, by a factor of 40 at a mass column of $\Sigma = 8$ g cm $^{-2}$, that of an X-ray source having $L_X = 2 \times 10^{30}$ erg s $^{-1}$ and $kT_X = 5$ keV. This model probably yields a hard upper limit on the stellar proton ionization rate, derived under a set of generous assumptions. Our $L_X = 10^{31}$ erg s $^{-1}$ case produces ionization rates ζ that approach those of the aforementioned model to within an order of magnitude. In any case we will see in Section 3.3.1 how our results can be scaled to any ζ .

Figure 1 depicts schematically how X-rays irradiate disk surface layers, usually pictured in the vertical direction as ensheathing the disk on its top and bottom faces. But in a transitional disk, a surface layer may also be present in the radial direction, at the rim of the central hole. We consider each of these environments in turn, estimating local number densities n_{H_2} [H $_2$ cm $^{-3}$] from the column density N [H $_2$ cm $^{-2}$] penetrated by X-rays.⁴

2.1.1. Surface Layers I: Top and Bottom Faces of a Conventional Flared Disk

When considering the surface layers of a conventional non-transitional disk, we describe our results as a function of the vertical column density N of hydrogen molecules, measured perpendicular to and toward the disk midplane. Thus our N coincides with N_\perp of IG, save for a factor of 2 because IG count hydrogen nuclei whereas we count hydrogen molecules. An equivalent measure of vertical column density N is the mass surface density $\Sigma \equiv N\mu$, where $\mu \approx 4 \times 10^{-24}$ g is the mean molecular weight of gas.

⁴ In this paper, ionization rates ζ , column densities N , and fractional densities x are referred to hydrogen molecules, not hydrogen nuclei.

³ A minority of sources surveyed by *Chandra* exhibited superhot X-ray flares with peak $L_X \sim 10^{32}$ erg s $^{-1}$ and $kT_X \sim 15$ keV (Getman et al. 2008a; Getman et al. 2008b). The degree to which superhot flares enhance ionization rates depends on the uncertain flare duty cycle. Because only $\sim 10\%$ of the *Chandra* sources flared once or twice over a 15-day observing period, and because each flare lasted less than ~ 1 day, the extra ionization from superhot flares may be modest.

TABLE 1
 MODEL PARAMETERS.

Parameter	Variable	Value	Reference
Disk radius	a	3, 30 AU	...
X-ray source luminosity ^a	L_X	10^{29} (10^{31}) erg s ⁻¹	Section 2.1
X-ray source temperature	kT_X	3 keV	Section 2.1
Cosmic-ray ionization rate	ζ_{CR}	0, (0.25×10^{-17}) s ⁻¹	Caselli et al. (1998)
Initial CO abundance ^b	x_{CO}	10^{-4}	Aikawa et al. (1996)
Total metal abundance ^{a,b}	x_M	10^{-8} (0, 10^{-6})	Section 2.4.1
Total grain abundance ^b	x_{grain}	$6 \times 10^{-15} \epsilon_{grain}$	Section 2.4.2
Grain settling (depletion) factor	ϵ_{grain}	$10^{-3} \leq \epsilon_{grain} \leq 10^{-1}$	Section 2.4.2
Total PAH abundance ^b	x_{PAH}	$10^{-6} \epsilon_{PAH}$	Section 2.4.3
PAH depletion factor	ϵ_{PAH}	$10^{-5} \leq \epsilon_{PAH} \leq 10^{-2}$	Section 2.4.3
Central stellar mass	M_*	$1 M_\odot$...
Gas temperature	T	80, 30 K	Section 2.2

^a Values in parentheses correspond to test cases different from our standard model.

^b All abundances are relative to H₂ by number.

To good approximation, the local number density

$$n_{H_2} \approx N/h \quad (3)$$

where the vertical scale height $h = c_s/\Omega = (kT/\mu)^{1/2}/\Omega$. For gas temperature $T \approx 80(30)$ K at $a = 3(30)$ AU (see Section 2.2 for how we derive these temperatures), we find $h = 0.09(1.8)$ AU.

Equation (3) underpins all our calculations of chemical equilibrium. For a typical $N \sim 10^{23}$ H₂ cm⁻², we have $n \sim 7 \times 10^{10}$ (4×10^9) H₂ cm⁻³ at $a = 3(30)$ AU.

2.1.2. Surface Layers II: Gap Rim of Transitional Disk

We assume that the gap rim is not shadowed from the star by gas interior to the rim. We cannot prove that the rim is not shadowed, but disk models based on the infrared SED suggest it is not (e.g., Calvet et al. 2005). Possibly gas at the rim wall ‘‘puffs up’’ because it is heated by X-rays and can maintain a larger vertical height than gas inside the hole (e.g., Dullemond et al. 2001).

For the case of the rim of a transitional disk, we reinterpret N (equivalently Σ) as the radial column of hydrogen molecules traversed by X-rays (Figure 1). To estimate the local number density n_{H_2} , we need to know the radial lengthscale ℓ over which material at the rim wall is distributed. Plausibly $h \lesssim \ell \lesssim a$. Chiang & Murray-Clay (2007) take $\ell \sim a$, but models based on SEDs and images suggest the rim is much sharper. Here we assume that $\ell \sim h$ so that Equation (3) applies equally well to transitional disks as to conventional disks—keeping in mind that N should be measured radially for the former and vertically for the latter.

To calculate ionization rates in the rim, we still use the results of IG, reinterpreting their N_\perp in their Figure 3 as our radial column N . Clearly the scattering geometry differs between the case of a transitional disk rim and the case of the top and bottom faces of IG’s conventional disk. Where material is optically thin to stellar X-rays, the two cases match in ionization rate (per molecule), but where it is optically thick, we underestimate the ionization rate in transitional disk rims by using IG because more X-rays escape by scattering vertically out of conventional disk surface layers than from the rim. Another reason we underestimate the ionization rate at high column density is because the total X-ray

flux per unit surface area of the disk is lower for conventional surface layers—which are illuminated at grazing incidence—than for the rim, which is illuminated at normal incidence. Nevertheless we estimate that these errors are of the order of unity, insofar as the columns that might possibly be MRI-active are not too optically thick to X-rays (Section 3.3), because the Thomson scattering phase function is fairly isotropic, and the cross-section for scattering is only comparable to that for photoionization at the relevant photon energies. In any case we will explore the effects of higher ionization rates by running a model with higher $L_X = 10^{31}$ erg s⁻¹ (Section 3.3.1).

2.2. Gas Temperature

The surface layers of protoplanetary disk atmospheres vary widely in temperature, from ~ 5000 K at the lowest columns where stellar X-rays heat the gas, down to $\lesssim 100$ K at the highest columns where dust reprocesses optical starlight. We draw our temperatures from the thermal model of Glassgold et al. (2004), which in turn is based on the dust temperature model of D’Alessio et al. (1999). At $a = 1$ AU at column densities of interest ($N \gtrsim 10^{22}$ cm⁻²), thermal balance is controlled primarily by reprocessing of starlight by dust, and gas and dust temperatures are nearly equal at ~ 130 K (Glassgold et al. 2004, their Figure 2). We adjust this result for the disk radii of our standard model using the dust temperature scaling law for the midplane of a passive flared disk, $T \propto a^{-3/7}$ (e.g., Chiang & Goldreich 1997). Thus at $a = 3$ AU we have $T = 80$ K, and at $a = 30$ AU we have $T = 30$ K. Note that these temperatures are lower—and arguably more realistic—than those assumed by BG and TCS, who invoked temperatures of the traditional Hayashi nebula without justification.

2.3. Chemical Network

Following Ilgner & Nelson (2006, hereafter IN), CMC, and BG, we apply a simple network of chemical reactions based on that designed for molecular clouds by Oppenheimer & Dalgarno (1974, hereafter OD). Ilgner & Nelson (2006) and BG compared the results of OD-based schemes to those of more complex networks extracted from the UMIST (University of Manchester Institute of Science and Technology; Woodall et al. 2007, hereafter

W07; Vasyunin et al. 2008) database. Fractional electron abundances derived by IN using the simple network were greater than those derived using the complex network, whereas BG, who used a more recent version of the UMIST database, found that the sign of the difference varied from case to case. The magnitude of the difference ranged up to a factor of 10, but was often $\lesssim 3$. Using the simple network seems the most practical approach, if we are content with order-of-magnitude answers. In Section 3.4, we test the results of our code against those of BG and TCS.

All reactions in our OD-based network are listed in Table 2 and shown schematically in Figure 2. Rate coefficients and their temperature dependences are taken from the UMIST database. The chain of events basically proceeds as follows. X-rays ionize H_2 to H_2^+ , which rapidly reacts with H_2 to produce H_3^+ . The H_3^+ ion combines with CO to form HCO^+ . Most HCO^+ ions dissociatively recombine with free electrons, but some transfer their charge to gas-phase metal atoms such as Mg. Free metals tend to be abundant positive charge carriers, as they recombine with free electrons only by a slow radiative channel. Charged particles in the network (e^- , H_3^+ , HCO^+ , metal $^+$) can neutralize by collisionally transferring their charge to PAHs and grains. The collisional charging process is described in Section 2.5.

The reaction loop is closed by the formation of H_2 on grain surfaces. To compute the rate of this reaction, we take neutral H atoms to collide with grains using the geometrical cross section for grains, and adopt from BG the uniform probability $\eta = 10^{-3}$ for a pair of adsorbed hydrogen atoms to form a hydrogen molecule (see their Equation 27). The precise rate of this reaction is not important for us, as it only sets the equilibrium abundance of H, which is irrelevant for the ionization fraction, as long as $n_{\text{H}} \ll n_{\text{H}_2}$.

In their original study OD included ionization of He and reactions involving atomic and molecular oxygen. We neglect these for simplicity. Most reactions involving oxygen initiate with the formation of the hydroxyl ion ($\text{H}_3^+ + \text{O} \rightarrow \text{OH}^+$), which proceeds at a rate only comparable to the formation of HCO^+ , which we do account for. Thus our neglect of oxygen within the OD framework is not expected to alter our results for the fractional ionization by more than a factor of 2. In any case, in Section 3.4 we will compare our results with those of more complex networks considered by BG and TCS.

2.4. Properties and Abundances of Trace Species

The trace ingredients of our model include gas-phase metals (Section 2.4.1), a monodispersion of micron-sized grains (Section 2.4.2), and PAHs (Section 2.4.3).

2.4.1. Gas-phase Metals (Magnesium)

For gas-phase metals which serve importantly as electron donors (OD; Fromang et al. 2002), we are guided by Mg, whose solar abundance is 3.5×10^{-5} atoms per hydrogen nucleus (Lodders 2003). The fraction of Mg that is in the gas phase—neither incorporated into grain interiors nor adsorbed onto grain surfaces—might be at most 3–30% by number, its value in the diffuse interstellar medium (Jenkins 2009). In the dense environments of protoplanetary disks, the gas-phase fraction should be

much smaller because magnesium is used toward building grains.

Nominally, our model temperatures of 30–80 K are so low that almost all of the Mg not incorporated into grain interiors should be adsorbed onto grain surfaces, leaving behind only a tiny fraction in the gas phase (Turner et al. 2007, their Section 2.2; see also Equation 26 of BG). Just how tiny is uncertain, given how sensitive the adsorption fraction is to gas temperature, and how steep temperature gradients can be in disk surface layers (Glassgold et al. 2004). Turbulent mixing of hot, high altitude, normally metal-rich layers with cold, low altitude, normally metal-poor layers can also complicate matters (Turner et al. 2007; TCS).

We adopt a standard metal abundance of $x_{\text{M}} = 10^{-8}$ metal atoms per H_2 , which corresponds to a gas-phase fraction of $\sim 10^{-4}$ by number relative to solar. Our choice is similar to those of IN and BG. We also experiment with a metal-free case in which all metals have been adsorbed onto grain surfaces ($x_{\text{M}} = 0$), and a metal-rich case for which $x_{\text{M}} = 10^{-6}$. Although the metal-rich case is not especially realistic and is not justified by our model parameters—in particular our low gas temperatures—we consider it anyway because we would like to understand the effects of metals in principle, and to connect with other studies that consider similarly large metal abundances (CMC; Turner et al. 2007; TCS).

2.4.2. Grains

The number of grains per H_2 molecule is

$$x_{\text{grain}} = \frac{\mu}{\frac{4}{3}\pi s^3 \rho_s} \frac{\rho_{\text{dust}}}{\rho_{\text{gas}}}, \quad (4)$$

where $\mu \approx 4 \times 10^{-24}$ g is the mean molecular weight of gas and $\rho_{\text{dust}}/\rho_{\text{gas}}$ is the dust-to-gas mass ratio. For simplicity we consider grains of a single radius $s = 1 \mu\text{m}$ and internal density $\rho_s = 2 \text{g cm}^{-3}$. There is ample evidence that micron-sized grains abound in surface layers, both from mid-infrared spectra of silicate emission lines (e.g., Natta et al. 2007) and from scattered light images at similar wavelengths (e.g., McCabe et al. 2003).

The dust-to-gas ratio in surface layers may differ considerably from its value in the well-mixed diffuse interstellar medium (ISM):

$$\frac{\rho_{\text{dust}}}{\rho_{\text{gas}}} \equiv \epsilon_{\text{grain}} \frac{\rho_{\text{dust}}}{\rho_{\text{gas}}} \Big|_{\text{ISM}}, \quad (5)$$

where for the ISM of solar abundance $\rho_{\text{dust}}/\rho_{\text{gas}}|_{\text{ISM}} = 0.015$ (Lodders 2003). Based on model fits to observed far-infrared SEDs (Chiang et al. 2001; D’Alessio et al. 2006; Dullemond & Dominik 2004), there is consensus that surface layer grains directly illuminated by optical light from their host stars have settled toward the midplane into regions of denser gas. Thus $\epsilon_{\text{grain}} < 1$, but actual values are not known with certainty, because small changes in the SED resulting from small changes in the height of the dust photosphere imply large changes in gas density in a near-Gaussian atmosphere. For example, Figure 15 of D’Alessio et al. (2006) shows that changing the far-infrared SED by less than a factor of 2 changes ϵ_{grain} by a factor of 10.

Table 3 lists fitted values of ϵ_{grain} for some transitional disks, drawn from the literature. At best they are ac-

TABLE 2
CHEMICAL REACTIONS INCLUDING COLLISIONAL CHARGING OF PAHS AND GRAINS.

Number	Reaction	Rate Coefficient ^a	Value	Reference
1 ^b	$\text{H}_2 + h\nu \rightarrow \text{H}_2^+ + e^-$	ζ_X	Taken from radiative transfer model	IG
2	$\text{H}_2 + \text{Cosmic-ray} \rightarrow \text{H}_2^+ + e^-$	ζ_{CR}	$(1/4) \times 10^{-17} \text{ s}^{-1}$	C98
3	$\text{H}_2^+ + \text{H}_2 \rightarrow \text{H}_3^+ + \text{H}$	$\alpha_{\text{H}_2^+, \text{H}_2}$	2.1×10^{-9}	W07
4	$\text{H}_3^+ + \text{CO} \rightarrow \text{HCO}^+ + \text{H}_2$	$\alpha_{\text{H}_3^+, \text{CO}}$	1.7×10^{-9}	W07
5 ^c	$\text{M} + \text{H}_3^+ \rightarrow \text{M}^+ + \text{H}_2 + \text{H}$	$\alpha_{\text{M}, \text{X}^+}$	1.0×10^{-9}	W07
6	$\text{M} + \text{HCO}^+ \rightarrow \text{M}^+ + \text{H} + \text{CO}$	$\alpha_{\text{M}, \text{X}^+}$	2.9×10^{-9}	W07
7	$\text{H}_3^+ + e^- \rightarrow \text{H}_2 + \text{H}$	$\alpha_{\text{H}_3^+, e}$	$2.3 \times 10^{-8} (T/300\text{K})^{-0.52}$	W07
8	$\text{HCO}^+ + e^- \rightarrow \text{H} + \text{CO}$	$\alpha_{\text{HCO}^+, e}$	$2.4 \times 10^{-7} (T/300\text{K})^{-0.69}$	W07
9	$\text{M}^+ + e^- \rightarrow \text{M} + h\nu$	$\alpha_{\text{M}^+, e}$	$2.8 \times 10^{-12} (T/300\text{K})^{-0.86}$	W07
10	$\text{PAH}(Z) + e^- \rightarrow \text{PAH}(Z-1)$	$\alpha_{\text{PAH}, e}$	Section 2.5	DS
11 ^d	$\text{PAH}(Z) + \text{X}^+ \rightarrow \text{PAH}(Z+1)$	$\alpha_{\text{PAH}, \text{X}^+}$	Section 2.5	DS
12	$\text{grain}(Z) + e^- \rightarrow \text{grain}(Z-1)$	$\alpha_{\text{grain}, e}$	Section 2.5	DS
13	$\text{grain}(Z) + \text{X}^+ \rightarrow \text{grain}(Z+1)$	$\alpha_{\text{grain}, \text{X}^+}$	Section 2.5	DS
14	$\text{PAH}(Z=-1) + \text{PAH}(Z=1) \rightarrow 2 \times \text{PAH}(Z=0)$	$\alpha_{\text{PAH}, \text{PAH}}$	Section 2.5	DS
15	$\text{H} + \text{H} + \text{grain} \rightarrow \text{H}_2 + \text{grain}$	$\alpha_{\text{physisorption}}$	Section 2.3	BG

^a ζ has units of s^{-1} and α has units of $\text{cm}^3 \text{s}^{-1}$.

^b $h\nu$ denotes a photon.

^c M represents a gas-phase atomic metal, e.g., Mg.

^d X^+ can be either H_3^+ , HCO^+ , or M^+ .

curate to order of magnitude. For our calculations we consider $10^{-3} \leq \epsilon_{\text{grain}} \leq 10^{-1}$ (Table 1).

TABLE 3
DUST SETTLING PARAMETER ϵ_{grain} FOR SOME TRANSITIONAL DISKS

Source	ϵ_{grain}	Reference
LkCa 15	10^{-3}	Espaillat et al. (2007a); Chiang et al. (2001)
UX Tau A	10^{-2}	Espaillat et al. (2007a)
CS Cha	10^{-2}	Espaillat et al. (2007b)
GM Aur	10^{-1}	Calvet et al. (2005)
DM Tau	10^{-1}	Calvet et al. (2005)

2.4.3. PAHs

For simplicity we model PAHs as spheres, each having a radius $s = 6\text{\AA}$ and internal density $\rho_s = 2 \text{ g cm}^{-3}$. Although in reality carbon atoms in PAHs are arranged in sheets and not spheres (e.g., Allamandola et al. 1999), the difference in cross section arising from geometry is only on the order of unity. Each of our model PAHs has about as much mass as a real PAH containing $N_C = 100$ carbon atoms. A PAH of this size is estimated to be just large enough to survive photo-destruction around Herbig Ae stars (Visser et al. 2007).

The central wavelengths of PAH emission lines from Herbig Ae/Be (HAe/Be) disks are observed to trend with the effective temperatures of their host stars (Sloan et al. 2005; Keller et al. 2008). This correlation indicates that PAHs in disks are not merely PAHs from the diffuse ISM transported unadulterated into circumstellar environments. Rather, PAHs in disks have been photo-processed, their chemical bonds altered by radiation from host stars. Possibly PAHs are continuously created and destroyed by local processes, e.g., sublimation of grain mantles and photodestruction (Keller et al. 2008). In this paper we do not account explicitly for such processes, i.e., we do not attempt to calculate the abundance of PAHs from first principles. Rather we fix the abundance of

PAHs using observations, as detailed in the remainder of this subsection.

Emission from PAHs is detected in an order-unity fraction of HAe/Be stars, but is rarely seen in T Tauri stars (e.g., Geers et al. 2006, hereafter G06). In principle this could mean that PAHs are less abundant in T Tauri disks, but the more likely explanation is that this is an observational selection effect: Herbig Ae/Be stars are more luminous in the ultraviolet (UV) and therefore cause their associated PAHs to fluoresce more strongly (see, e.g., Figure 9 of G06, which shows how the PAH intensity drops below the *Spitzer* detection threshold with decreasing stellar effective temperature). Another clue that PAHs are just as abundant in T Tauri disks as in HAe/Be disks is that those few T Tauri stars with positive PAH detections tend to have unusually low mid-infrared continua, allowing PAH emission lines to stand out more clearly (G06). In other words, those T Tauri systems where PAHs have been detected are transitional systems, and their PAH abundances seem no different than in their HAe/Be counterparts.

Geers et al. (2006) used radiative transfer models to fit the intensities of the $11.2 \mu\text{m}$ PAH fluorescence line in eight Herbig Ae and T Tauri disks, concluding that the PAH abundance is 10^{-7} – 10^{-8} per H_2 (see their Figure 9). This result is highly model dependent. Perhaps the chief source of uncertainty lies in the grain opacity. Inferred PAH abundances relative to gas are sensitive to assumptions about the local grain size distribution and dust-to-gas ratio because the soft ultraviolet radiation (~ 1000 – 3000\AA wavelength) which causes PAHs to fluoresce is also absorbed by ambient grains. Thus the intensity of PAH emission depends on how many grains are competing with PAHs for the same illuminating photons. The grain opacity, in turn, decreases by orders of magnitude as dust settles (Section 2.4.2). Because G06 did not account for dust sedimentation and instead assumed the dust-to-gas ratio in disks was similar to that of the well-mixed ISM, the PAH abundances relative to

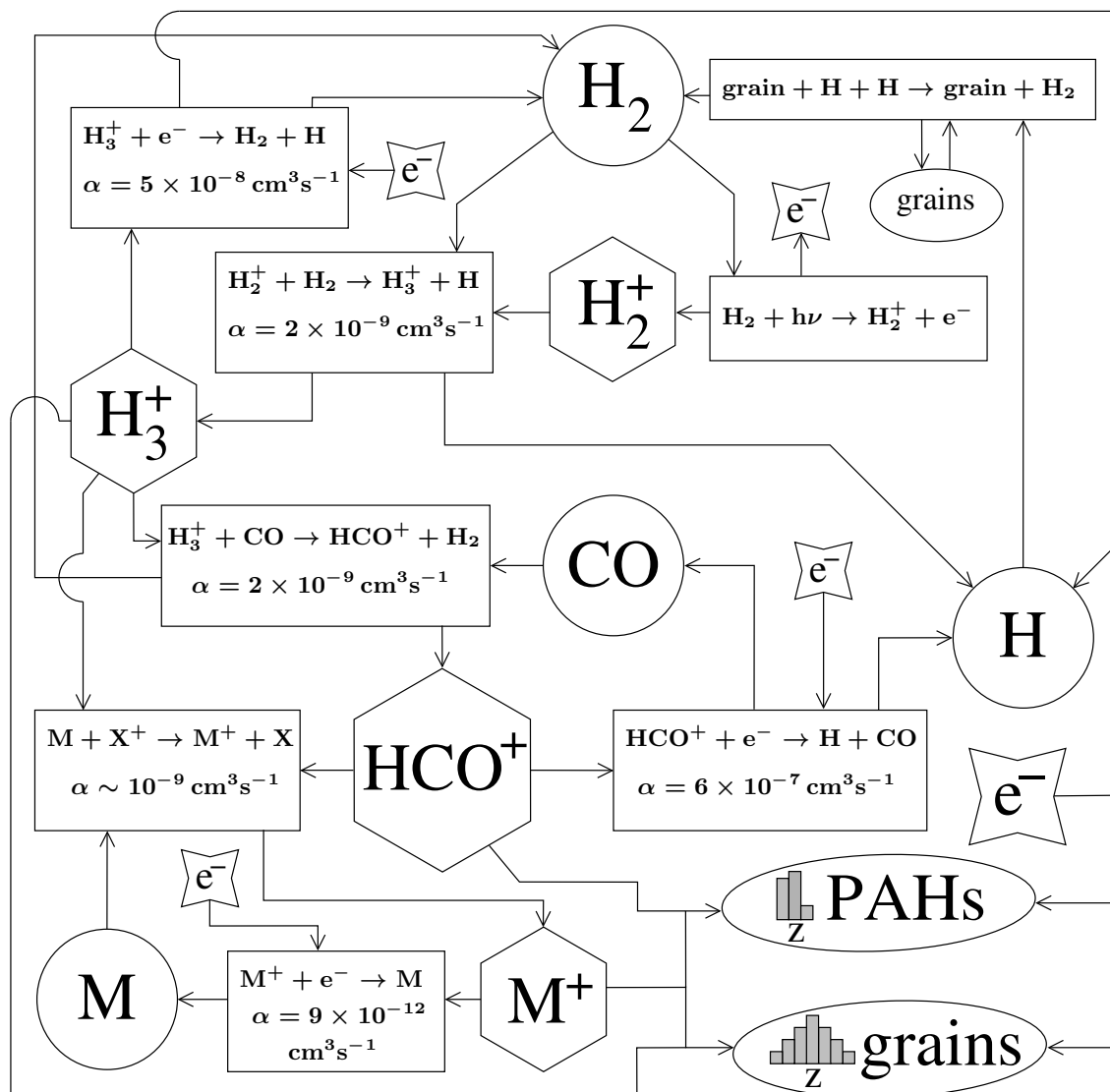


FIG. 2.— Our chemical reaction network, derived from Oppenheimer & Dalgarno (1974). Rate coefficients as shown in this Figure are evaluated at $T = 80$ K. See Table 2 for a comprehensive list of all modeled reactions and precise rate coefficients.

gas that they computed are actually upper limits. Surface layer grains have likely settled toward the midplane into regions of high gas density, and were the local PAH abundance to remain as inferred at 10^{-7} – 10^{-8} per H_2 , the ratio of PAH line intensity to dust continuum would be larger than observed (Dullemond et al. 2007).

In our model the number of PAHs per H_2 is

$$x_{\text{PAH}} \equiv \epsilon_{\text{PAH}} \times 10^{-6}, \quad (6)$$

where $\epsilon_{\text{PAH}} < 1$ measures how depleted PAHs are in disk surface layers relative to PAHs in the diffuse ISM (Li & Draine 2001). Based on the considerations above, we should combine the G06 depletion factor of 0.01–0.1 with the grain depletion factor $\epsilon_{\text{grain}} \sim 0.001$ –0.1, which parameterizes the reduction of dust opacity due to dust sedimentation. We thus estimate that $10^{-5} \lesssim \epsilon_{\text{PAH}} \lesssim 10^{-2}$ (Table 1). In our calculations we select the parameter combinations $(\epsilon_{\text{grain}}, \epsilon_{\text{PAH}}) = (10^{-1}, 10^{-2})$ and $(\epsilon_{\text{grain}}, \epsilon_{\text{PAH}}) = (10^{-3}, 10^{-5})$ which bracket the range of possibilities.

A final point to consider is whether the observed PAHs are present at the same column depths that are relevant for X-ray driven MRI. The X-ray stopping column should be compared with the column that presents optical depth unity to the soft UV radiation driving PAH emission. In the model of G06 in which dust has not settled, photons at wavelengths of 1000–3000 Å are stopped by submicron-sized silicate/carbonaceous grains within a hydrogen column of $\sim 0.005 \text{ g cm}^{-2}$ (V. Geers, private communication, 2010; see also Habart et al. 2004 who used similar dust opacities). After we account for grain settling (ϵ_{grain}), the UV absorption column increases to ~ 0.05 – 5 g cm^{-2} . Although model-dependent, our estimate of the UV absorption column corresponds well to X-ray stopping columns, and thus to columns that might possibly be MRI-active.

2.5. Collisional Charging of PAHs and Grains

Grains and PAHs are modeled as conducting spheres for simplicity. Electrons and ions collide with and stick to grains and PAHs, charging them. When the total electron capture rate by grains and PAHs matches the total ion capture rate, the distribution of charges carried by PAHs and grains reaches dynamical equilibrium. The average charge state on a PAH/grain $\langle Z \rangle < 0$ because in thermal equilibrium electrons move more quickly than ions. Convenient and readily derived approximations for $\langle Z \rangle$ in various limits were given by Draine & Sutin (1987, hereafter DS). We will find that $\langle Z \rangle$ ranges between -1 and 0 for our PAHs of radius 6Å , while for our micron-sized grains $\langle Z \rangle \approx -22$. The remainder of this subsection details how we compute the electron and ion capture rates.

The rates at which ions or electrons collide with PAHs or grains are enhanced by Coulomb focusing between static charges, as well as by the induced dipole force (Natanson 1960; Robertson & Sternovsky 2008). The cross sections can be derived from kinetic theory by considering the potential between a conducting sphere of radius s and charge Ze , located at a distance r from a charge q :

$$\phi(Z, r) = \frac{qZe}{r} - \frac{q^2s^3}{2r^2(r^2 - s^2)} \quad (7)$$

(e.g., Jackson 1975). The first term is the usual monopole interaction, while the second arises from the induced dipole (image charges). For a neutral sphere, the velocity-dependent cross section derives from applying conservation of energy and momentum to the second term of (7). Multiplying this cross section by either the electron or ion velocity, and averaging over a Maxwellian speed distribution at temperature T , yields the rate coefficient (units of $\text{cm}^3 \text{ s}^{-1}$)

$$\alpha = \pi s^2 Sc \left(1 + \sqrt{\frac{\pi q^2}{2skT}} \right) \quad \text{for } Ze/q = 0 \quad (8)$$

where k is the Boltzmann constant, $c = \sqrt{8kT/\pi m}$ is the mean speed for either electrons of mass $m = m_e$ or ions of mass $m = m_{\text{X}^+}$, and S is the probability that the electron/ion sticks to the PAH/grain. We will discuss the sticking coefficient S shortly.

For a charged sphere, the cross section is enhanced by both terms in (7). There is no analytical solution for this case, but DS provided the following approximate formulae:

$$\alpha = \pi s^2 Sc [1 - Ze/(q\tau)] (1 + \sqrt{2/(\tau - 2Ze/q)}) \quad \text{for } Ze/q < 0 \quad (9)$$

$$\alpha = \pi s^2 Sc [1 + (4\tau + 3Ze/q)^{-1/2}]^2 \exp(-\beta/\tau) \quad \text{for } Ze/q > 0 \quad (10)$$

where $\tau \equiv skT/q^2$,

$$\beta \equiv \frac{Ze}{qg} - \frac{1}{2g^2(g^2 - 1)}, \quad (11)$$

and g is the solution to the transcendental equation

$$\frac{2g^2 - 1}{g(g^2 - 1)^2} = \frac{Ze}{q}. \quad (12)$$

Upon colliding with a PAH or grain, the electron or ion sticks with probability S . For ions, we set $S = S_{\text{X}^+} = 1$ (DS; IN; BG). For electrons colliding with PAHs, $S = S_e$ depends on the detailed molecular structure of the PAH. Allamandola et al. (1989) calculated how the electron sticking coefficient increases with both the number of carbon atoms and the electron affinity. The dependence on electron affinity is especially strong. A PAH having $N_C = 32$ and an electron affinity of 0.7 eV has $S_e \approx 3 \times 10^{-5}$ (see their Figure 25), while the same-sized PAH with an electron affinity of 1 eV has $S_e \approx 10^{-2}$ (see page 769 of their paper). Estimated electron affinities of real $N_C = 32$ PAHs (e.g., ovalene and hexabenzocoronene) exceed 1 eV. Allamandola et al. (1989) stated that “only for pericondensed PAHs [which are more stable than catacondensed PAHs] containing considerably more than 20 C atoms will the electron sticking coefficient approach unity.” Based on these considerations, we take $S_e = 0.1$ for our $N_C = 100$ PAHs. For the much larger grains we set $S_e = 1$.

In our code, the range of charges a grain can possess extends from $Z = -200$ to $+200$. We have verified that this range is large enough to accommodate the entire equilibrium charge distribution, which for our μm -sized grains peaks at -22 (see Figure 4). Accounting only for a few charges—up to $|Z| = 3$ as did Sano et al. (2000), IN, BG, and TCS—is not necessarily adequate for micron-sized grains which have fairly large capacitances. For

PAHs we consider charges Z between -16 and $+16$. Most PAHs will turn out to have either $Z = 0$ or -1 . Because of their smaller size, a single PAH will be less charged than a single grain; electrons collide less frequently with a negatively charged sphere as the radius of the sphere decreases and the Coulomb potential steepens.

We neglect adsorption of neutral gas-phase species onto grain surfaces, and any mass increase of grains and PAHs from collisions with ions. Grain-grain and PAH-grain collisions are negligible and ignored. We do account for the possibility that a PAH with a single negative charge can neutralize by colliding with a PAH with a single positive charge (reaction 14 in Table 2), though in practice this reaction is not significant.

2.6. Numerical Method of Solution

The time-dependent rate equations for the abundances of species are readily constructed from the reactions listed in Table 2. For example, the number density of electrons n_e obeys

$$\begin{aligned} \frac{dn_e}{dt} = & n_{\text{H}_2} \zeta - n_e \sum_{\text{X}^+} \alpha_{\text{X}^+,e} n_{\text{X}^+} \\ & - n_e \sum_{Z=-16}^{16} \alpha_{\text{PAH},e} n_{\text{PAH}} \\ & - n_e \sum_{Z=-200}^{200} \alpha_{\text{grain},e} n_{\text{grain}} \end{aligned} \quad (13)$$

where the index X^+ runs over reactions 7, 8, and 9 in Table 2. The first sum over Z occurs over the charge states of PAHs, while the second sum occurs over the charge states of grains, with rate coefficients α given in Section 2.5.

The charge distributions of PAHs and grains are governed by recurrence equations (Parthasarathy 1976; Whitten et al. 2007), e.g., for PAHs:

$$\begin{aligned} \frac{dn_{\text{PAH},Z}}{dt} = & (n_{\text{PAH}} \alpha_{\text{PAH},e})_{Z+1} n_e \\ & + \sum_{\text{X}^+} (n_{\text{PAH}} \alpha_{\text{PAH},\text{X}^+})_{Z-1} n_{\text{X}^+} \\ & - (n_{\text{PAH}} \alpha_{\text{PAH},e})_Z n_e \\ & - \sum_{\text{X}^+} (n_{\text{PAH}} \alpha_{\text{PAH},\text{X}^+})_Z n_{\text{X}^+}. \end{aligned} \quad (14)$$

The right-hand side of Equation (14) accounts for all the ways in which PAHs of charge Z can be created or destroyed by collisions with electrons and ions (reactions 10 and 11 in Table 2). When $Z = \pm 1$, Equation (14) is supplemented by an extra loss term accounting for reaction 14.

All rate equations are discretized to first order and advanced simultaneously using a forward Euler algorithm with a fixed timestep $\Delta t \leq 1 \times 10^{-3}$ s. At $t = 0$, all PAHs and grains have $Z = 0$ and all hydrogen is in the form of H_2 . In principle we could simply advance the network forward until the system equilibrates, i.e., until the time rates of change of the abundances fall below some specified tolerance. However the reaction rates in our network

span almost 5 orders of magnitude. Thus, our equations are stiff and a brute-force integration would require an inordinate number of timesteps. Metals are typically the slowest constituent to reach equilibrium because they react with electrons only slowly by radiative recombination (reaction 9).

To circumvent the bottleneck posed by metals, we proceed as follows. We run R versions of the code having R evenly spaced initial abundances for charged metals n_{M^+} . For each run, we initially set $n_e = n_{\text{M}^+}$ to ensure charge neutrality. We run each code until the abundances of all species drift only because of slow changes in n_{M^+} . We evaluate dn_{M^+}/dt at the end of each run. The equilibrium value of n_{M^+} is bracketed by the two runs having opposing signs for dn_{M^+}/dt . We then start a new iteration with R runs having initial metal abundances evenly spaced between the two bounding runs of the previous iteration. In this way we refine our initial guesses for n_{M^+} until we arrive at two sets of initial conditions that differ by less than 30%. The equilibrium value of n_{M^+} we report lies at the intersection of the two curves for $n_{\text{M}^+}(t)$, linearly extrapolated forward in time. Other variables (n_e , n_{HCO^+} , and $n_{\text{H}_3^+}$) are also extrapolated. The number of runs R at each iteration varies from 2 to 5.

We use the time t_{eq} at which the two extrapolated curves for n_{M^+} intersect as an estimator of the equilibration time of the chemical network. For t_{eq} to be a robust estimator, it should be independent of initial conditions. We found that the value of t_{eq} remained constant to within a factor of 3 when initial conditions varied over 2 orders of magnitude. Our values for t_{eq} will be compared to dynamical timescales Ω^{-1} in Section 3.3.2.

Errors are estimated by monitoring conservation of charge and conservation of the total number density of PAHs + grains. Over 10^{10} timesteps, the charge remains constant (at zero) to better than one part in 10^8 , with similar results for the number density of PAHs + grains. As a test of our code, we reproduced the normalized charge distribution on PAHs computed by Jensen & Thomas (1991, see their Figure 2a).

3. RESULTS

In Section 3.1, we describe how charges distribute themselves on PAHs and grains in dynamical equilibrium. In Section 3.2, we explore how the free electron and ion abundances vary with increasing PAH abundance. In Section 3.3, we show what all this implies for the degree of magnetic coupling in disk surface layers, interpreting our numerical results whenever possible with simple analytic estimates. In that section we also compute timescales for the chemical network to equilibrate, and compare to the dynamical timescales over which the MRI may act. In Section 3.4, we test the validity of our simple network/code by seeing how closely we can reproduce the results of more complex networks/codes by BG and TCS.

3.1. Charge Distributions on PAHs and Grains

Figures 3 and 4 show the charge distributions on PAHs and grains, respectively, for the case $a = 3$ AU, $\Sigma = 0.3 \text{ g cm}^{-2}$, $x_{\text{M}} = 10^{-8}$ (standard metal abundance), $\epsilon_{\text{PAH}} = 10^{-5}$ (low PAH abundance), and $\epsilon_{\text{grain}} = 10^{-3}$ (low grain abundance). Most of the PAHs either have

$Z_{\text{PAH}} = 0$ or $Z_{\text{PAH}} = -1$. For grains, the average charge state (the peak of the distribution) is $\langle Z_{\text{grain}} \rangle \approx -22$. The shape of the charge distribution for grains approaches the Gaussian given by Equation (4.15) of DS.

We may understand $\langle Z \rangle$ simply. Consider the PAHs; identical considerations apply to grains. We take the limit that the dominant ions are metals and the limit that the total charge carried by PAHs is much less than the free charge. Together these limits imply that $x_e \approx x_{M^+}$. Then detailed balance between forward and reverse reaction rates dictates that (cf. Equation 14):

$$(n_{\text{PAH}} \alpha_{\text{PAH},e})_{Z+1} = (n_{\text{PAH}} \alpha_{\text{PAH},M^+})_Z. \quad (15)$$

From this equation it is evident that if ever the rate coefficients $(\alpha_{\text{PAH},e})_{Z+1}$ and $(\alpha_{\text{PAH},M^+})_Z$ were to be equal, the densities $(n_{\text{PAH}})_{Z+1}$ and $(n_{\text{PAH}})_Z$ would be equal, i.e., the charge distribution would be at an extremum. Thus we may estimate the average charge $\langle Z \rangle$ by merely plotting the rate coefficients α_{PAH,M^+} and $\alpha_{\text{PAH},e}$ against Z and seeing where the curves intersect. This exercise is performed in Figures 3 and 4. Indeed what the full numerical model gives for $\langle Z \rangle$ is close to the Z for which the curves for the rate coefficients intersect. (Of course, perfect agreement cannot be obtained because it is never strictly true that $(\alpha_{\text{PAH},e})_{Z+1} = (\alpha_{\text{PAH},M^+})_Z$.)

There is another, even simpler limit where $\langle Z \rangle$ may be estimated. In the extreme case that the gas is so saturated with grains or PAHs that practically no free charges are left, we must have $\langle Z \rangle \rightarrow 0$. Figure 5 shows the results of an experiment using our full code in which we increase ϵ_{PAH} until this regime is reached. For this Figure, the grain abundance is set to zero to isolate the effects of PAHs. Figure 6 is analogous; ϵ_{grain} is increased while the PAH abundance is held fixed at zero. Both figures follow the transition from $\langle Z \rangle \neq 0$ to $\langle Z \rangle \rightarrow 0$. Observationally inferred values for ϵ_{grain} (see the shaded region of Figure 6) are never so high as to cross into the $\langle Z_{\text{grain}} \rangle \rightarrow 0$ regime. By contrast, Figure 5 shows that PAHs may be sufficiently abundant in disks that they impact the density of free charges. The critical PAH abundance x_{PAH}^* dividing the $\langle Z_{\text{PAH}} \rangle \neq 0$ limit from the $\langle Z_{\text{PAH}} \rangle \rightarrow 0$ limit is the one for which an electron attaches itself to a PAH as frequently as it recombines with an ion. This critical abundance is discussed further in Section 3.2.

3.2. Ionization Fraction vs. PAH Abundance

Figure 7 plots the fractional electron and ion densities, x_e and x_i , against the PAH abundance x_{PAH} , for $a = 3$ AU, $\Sigma = 0.3 \text{ g cm}^{-2}$, $x_M = 10^{-8}$ (standard metal abundance), and $\epsilon_{\text{grain}} = 10^{-3}$ – 10^{-1} (see the figure caption for how ϵ_{grain} is assigned to each ϵ_{PAH}). Figure 8 is identical except that it considers the metal-rich case $x_M = 10^{-6}$. The primary ions in both cases are atomic metals and HCO^+ molecules. At low PAH abundances, charged metal ions are the most abundant. As the number of PAHs is increased, HCO^+ becomes the dominant ion. See Table 4 for a precise breakdown of component ion densities for our standard metal abundance case.

According to Figures 7 and 8, the electron and ion densities are nearly equal and constant with x_{PAH} as long as x_{PAH} is not too large. In going from the standard metal abundance of $x_M = 10^{-8}$ to the metal-rich case of $x_M = 10^{-6}$, the free charge abundance increases by

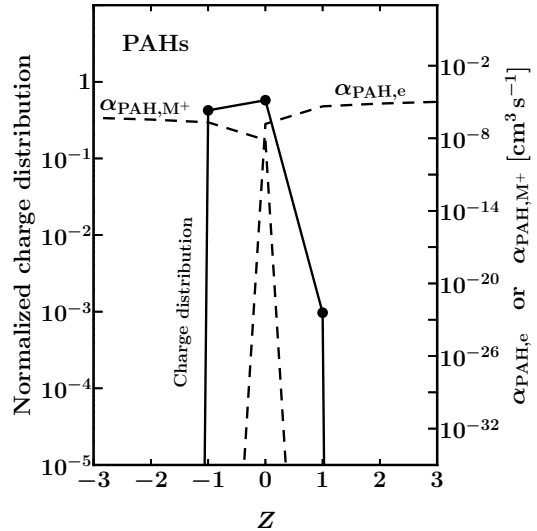


FIG. 3.— Equilibrium charge distribution on PAHs (solid circles, left axis) for $a = 3$ AU, $\Sigma = 0.3 \text{ g cm}^{-2}$, $x_M = 10^{-8}$ (standard metal abundance), $\epsilon_{\text{PAH}} = 10^{-5}$ (low PAH abundance), and $\epsilon_{\text{grain}} = 10^{-3}$ (low grain abundance). The distribution peaks at $Z = 0$, approximately where the attachment coefficients (dashed lines, right axis) for electrons with PAHs and metal ions with PAHs cross.

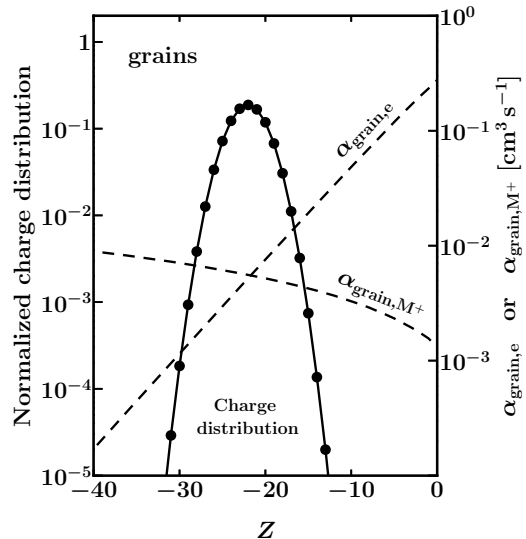


FIG. 4.— Same as Figure 3 but for grains.

an order of magnitude. Once x_{PAH} exceeds some critical abundance x_{PAH}^* , the electron and ion densities diverge—the ion density is higher, and the balance of negative charges is carried by PAHs. In the limit $x_{\text{PAH}} \gg x_{\text{PAH}}^*$, both the electron and ion densities decrease with increasing PAH abundance in an approximately inverse linear way. All of this behavior can be understood analytically as follows.

3.2.1. Analytical Model for Ionization Fraction vs. PAH Abundance

Our code's results for $x_e(x_{\text{PAH}})$, $x_i(x_{\text{PAH}})$, and x_{PAH}^* may be understood using the following simple model. The model consists only of X-rays, molecular hydrogen, electrons, PAHs, and one ion species—either HCO^+ for

TABLE 4
DENSITIES OF CHARGED SPECIES FOR OUR STANDARD MODEL ($x_M = 10^{-8}$, $L_X = 10^{29}$ erg s $^{-1}$)

$a = 3 \text{ AU}, \epsilon_{\text{PAH}} = 10^{-5}, \epsilon_{\text{grain}} = 10^{-3}$											
Σ	n_{H_2}	n_e	n_{M^+}	n_{HCO^+}	$n_{\text{H}_3^+}$	x_e	x_i	x_{PAH}	x_{grain}	$\langle Z_{\text{PAH}} \rangle$	$\langle Z_{\text{grain}} \rangle$
6×10^{-3}	1×10^9	2×10^1	1×10^1	8×10^0	5×10^{-1}	2×10^{-8}	2×10^{-8}	1×10^{-11}	6×10^{-18}	-4×10^{-1}	-22
4×10^{-2}	7×10^9	4×10^1	4×10^1	4×10^0	8×10^{-2}	6×10^{-9}	6×10^{-9}	1×10^{-11}	6×10^{-18}	-4×10^{-1}	-22
3×10^{-1}	5×10^{10}	3×10^1	3×10^1	1×10^0	3×10^{-3}	6×10^{-10}	6×10^{-10}	1×10^{-11}	6×10^{-18}	-4×10^{-1}	-22
2×10^0	4×10^{11}	1×10^1	1×10^1	4×10^{-1}	1×10^{-4}	4×10^{-11}	4×10^{-11}	1×10^{-11}	6×10^{-18}	-4×10^{-1}	-22
1×10^1	2×10^{12}	6×10^{-1}	3×10^0	3×10^{-2}	6×10^{-6}	2×10^{-13}	1×10^{-12}	1×10^{-11}	6×10^{-18}	-1×10^{-1}	-15
6×10^1	1×10^{13}	7×10^{-4}	5×10^{-3}	2×10^{-5}	3×10^{-9}	6×10^{-17}	4×10^{-16}	1×10^{-11}	6×10^{-18}	-4×10^{-5}	-14
$a = 3 \text{ AU}, \epsilon_{\text{PAH}} = 10^{-2}, \epsilon_{\text{grain}} = 10^{-1}$											
Σ	n_{H_2}	n_e	n_{M^+}	n_{HCO^+}	$n_{\text{H}_3^+}$	x_e	x_i	x_{PAH}	x_{grain}	$\langle Z_{\text{PAH}} \rangle$	$\langle Z_{\text{grain}} \rangle$
6×10^{-3}	1×10^9	1×10^1	5×10^{-1}	1×10^1	5×10^{-1}	9×10^{-9}	1×10^{-8}	1×10^{-8}	6×10^{-16}	-4×10^{-1}	-21
4×10^{-2}	7×10^9	5×10^0	1×10^0	2×10^1	8×10^{-2}	7×10^{-10}	2×10^{-9}	1×10^{-8}	6×10^{-16}	-2×10^{-1}	-17
3×10^{-1}	5×10^{10}	2×10^{-1}	7×10^{-1}	3×10^0	3×10^{-3}	4×10^{-12}	8×10^{-11}	1×10^{-8}	6×10^{-16}	-8×10^{-3}	-9
2×10^0	4×10^{11}	1×10^{-2}	7×10^{-2}	2×10^{-1}	1×10^{-4}	4×10^{-14}	8×10^{-13}	1×10^{-8}	6×10^{-16}	-8×10^{-5}	-9
1×10^1	2×10^{12}	6×10^{-4}	4×10^{-3}	1×10^{-2}	6×10^{-6}	3×10^{-16}	6×10^{-15}	1×10^{-8}	6×10^{-16}	-1×10^{-7}	-9
6×10^1	1×10^{13}	3×10^{-7}	2×10^{-6}	5×10^{-6}	3×10^{-9}	2×10^{-20}	6×10^{-19}	1×10^{-8}	6×10^{-16}	-1×10^{-10}	-3×10^{-3}
$a = 30 \text{ AU}, \epsilon_{\text{PAH}} = 10^{-5}, \epsilon_{\text{grain}} = 10^{-3}$											
Σ	n_{H_2}	n_e	n_{M^+}	n_{HCO^+}	$n_{\text{H}_3^+}$	x_e	x_i	x_{PAH}	x_{grain}	$\langle Z_{\text{PAH}} \rangle$	$\langle Z_{\text{grain}} \rangle$
6×10^{-3}	6×10^7	5×10^{-1}	4×10^{-1}	1×10^{-1}	7×10^{-3}	9×10^{-9}	9×10^{-9}	1×10^{-11}	6×10^{-18}	-3×10^{-1}	-9
4×10^{-2}	4×10^8	9×10^{-1}	9×10^{-1}	4×10^{-2}	8×10^{-4}	2×10^{-9}	2×10^{-9}	1×10^{-11}	6×10^{-18}	-3×10^{-1}	-9
3×10^{-1}	3×10^9	4×10^{-1}	4×10^{-1}	2×10^{-2}	2×10^{-5}	2×10^{-10}	2×10^{-10}	1×10^{-11}	6×10^{-18}	-3×10^{-1}	-9
2×10^0	2×10^{10}	1×10^{-1}	2×10^{-1}	6×10^{-3}	1×10^{-6}	8×10^{-12}	1×10^{-11}	1×10^{-11}	6×10^{-18}	-3×10^{-1}	-9
1×10^1	1×10^{11}	7×10^{-3}	5×10^{-2}	4×10^{-4}	7×10^{-8}	7×10^{-14}	4×10^{-13}	1×10^{-11}	6×10^{-18}	-4×10^{-2}	-6
6×10^1	6×10^{11}	3×10^{-6}	5×10^{-5}	2×10^{-7}	3×10^{-11}	5×10^{-18}	1×10^{-16}	1×10^{-11}	6×10^{-18}	-8×10^{-6}	-4
$a = 30 \text{ AU}, \epsilon_{\text{PAH}} = 10^{-2}, \epsilon_{\text{grain}} = 10^{-1}$											
Σ	n_{H_2}	n_e	n_{M^+}	n_{HCO^+}	$n_{\text{H}_3^+}$	x_e	x_i	x_{PAH}	x_{grain}	$\langle Z_{\text{PAH}} \rangle$	$\langle Z_{\text{grain}} \rangle$
6×10^{-3}	6×10^7	2×10^{-1}	9×10^{-3}	3×10^{-1}	7×10^{-3}	3×10^{-9}	5×10^{-9}	1×10^{-8}	6×10^{-16}	-2×10^{-1}	-8
4×10^{-2}	4×10^8	5×10^{-2}	2×10^{-2}	3×10^{-1}	8×10^{-4}	1×10^{-10}	8×10^{-10}	1×10^{-8}	6×10^{-16}	-7×10^{-2}	-6
3×10^{-1}	3×10^9	2×10^{-3}	9×10^{-3}	3×10^{-2}	2×10^{-5}	7×10^{-13}	2×10^{-11}	1×10^{-8}	6×10^{-16}	-2×10^{-3}	-4
2×10^0	2×10^{10}	1×10^{-4}	8×10^{-4}	2×10^{-3}	1×10^{-6}	7×10^{-15}	2×10^{-13}	1×10^{-8}	6×10^{-16}	-2×10^{-5}	-4
1×10^1	1×10^{11}	8×10^{-6}	5×10^{-5}	1×10^{-4}	7×10^{-8}	7×10^{-17}	2×10^{-15}	1×10^{-8}	6×10^{-16}	-1×10^{-9}	-3
6×10^1	6×10^{11}	3×10^{-9}	2×10^{-8}	5×10^{-8}	3×10^{-11}	5×10^{-21}	1×10^{-19}	1×10^{-8}	6×10^{-16}	-1×10^{-10}	-2×10^{-3}

NOTE. — The surface density Σ has units of g cm $^{-2}$; number densities n have units of cm $^{-3}$; and fractional densities x are measured per H $_2$. The ion density $x_i = x_{\text{M}^+} + x_{\text{HCO}^+}$.

our standard metal abundance case, or ionized metals M $^+$ for the metal-rich case. In the simplified model, X-ray ionization of a hydrogen molecule produces a free electron and—skipping the entire reaction chain—one ion. The system reduces to the rate equations

$$\frac{dn_e}{dt} = \zeta n_{\text{H}_2} - n_e n_i \alpha_{i,e} - n_e x_{\text{PAH}} n_{\text{H}_2} (\alpha_{\text{PAH},e})_{\langle Z \rangle} \quad (16)$$

$$\frac{dn_i}{dt} = \zeta n_{\text{H}_2} - n_i n_e \alpha_{i,e} - n_i x_{\text{PAH}} n_{\text{H}_2} (\alpha_{\text{PAH},i})_{\langle Z \rangle} \quad (17)$$

for the electron and ion densities, n_e and n_i . The subscript i denotes either HCO $^+$ or M $^+$.

In the simplified model, all PAHs with abundance $x_{\text{PAH}} n_{\text{H}_2}$ are assumed to be identically charged. We set this common charge equal to the average charge state $\langle Z \rangle$, results for which were given in Section 3.1.

We exclude our large, micron-sized grains from the analytic model. Although these grains were useful for infer-

ring PAH abundances from observations (Section 2.4.3), their collective surface area is too low to significantly influence the electron chemistry in any of our model runs. Of course, because PAHs and grains are both modeled the same way, i.e., as spherical conductors, all of the equations below would still be valid were we to replace PAHs with grains.

Standard metal abundance. — As stated above, we assume for this case that all ions are HCO $^+$ molecules and neglect M $^+$. We may solve for x_e and $x_i = x_{\text{HCO}^+}$ in the limits of low and high PAH abundance. In the limit of low x_{PAH} , the rightmost terms in Equations (16) and (17) can be

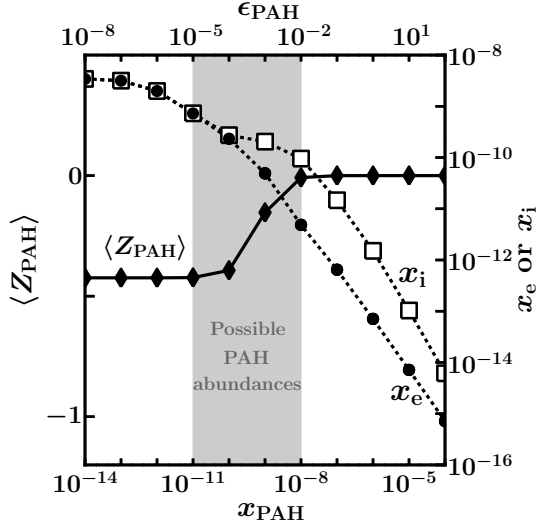


FIG. 5.— Average charge state of PAHs as a function of PAH abundance (solid diamonds, left axis). Dashed lines show simulation results for fractional electron abundance x_e (solid circles, right axis) and fractional ion abundance x_i (open squares, right axis). The shaded region marks observationally inferred PAH abundances, measured by number either relative to H_2 (x_{PAH} , bottom axis) or relative to the PAH abundance in the diffuse ISM (depletion factor $\epsilon_{\text{PAH}} \equiv x_{\text{PAH}}/10^{-6}$, top axis). Parameters for this run are $a = 3$ AU, $x_{\text{M}} = 10^{-8}$, $\Sigma = 0.3$ g cm^{-2} , and $\epsilon_{\text{grain}} = 0$ (kept at zero to isolate the effect of PAHs). The shift to $\langle Z_{\text{PAH}} \rangle = 0$ occurs when there are so many PAHs that they begin to adsorb most of the free charge. At this point x_i and x_e diverge; see also Figure 7.

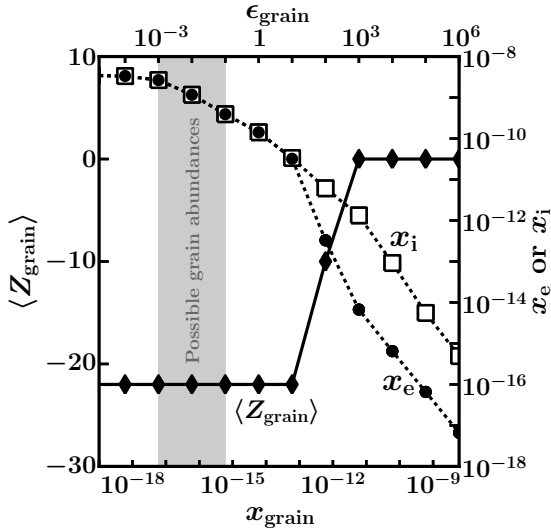


FIG. 6.— Same as Figure 5 but for grains. Parameters for this run are $a = 3$ AU, $x_{\text{M}} = 10^{-8}$, $\Sigma = 0.3$ g cm^{-2} , and $\epsilon_{\text{PAH}} = 0$ (kept at zero to isolate the effect of grains). Our grains all have radii of $1 \mu\text{m}$, which is so large that their corresponding abundance as inferred from observation (shaded region) is too low to significantly affect the amount of free charge.

ignored, yielding in steady state:

$$x_e = x_{\text{HCO}^+} = \sqrt{\zeta/n_{\text{H}_2}\alpha_{\text{HCO}^+,e}} \quad (18)$$

$$\sim 10^{-10} \left(\frac{L_X}{10^{29} \text{ erg s}^{-1}} \right)^{1/2} \times \left(\frac{\Sigma}{0.3 \text{ g cm}^{-2}} \right)^{-1/2} \left(\frac{a}{3 \text{ AU}} \right)^{-0.5} \quad (19)$$

for standard metals and low PAHs.

In going from Equations (18) to (19) we account for the distance dependence of temperature but assume material is optically thin to X-rays. The square-root law of Equation (18) is often used by other workers (e.g., Gammie 1996; Glassgold et al. 1997). It is plotted as a horizontal dashed line in Figure 7, and should be compared with the curves for x_e and x_i from our code, plotted as solid lines. In the limit of low x_{PAH} , the electron and ion abundances computed from the code are nearly constant with x_{PAH} , as predicted by the analytic model. However, the results from the code sit above the line for Equation (18) by about an order of magnitude. The factor of 10 offset arises because Equation (18) ignores ionized metals, which recombine with electrons much more slowly than does HCO^+ and which remain abundant compared to HCO^+ in our standard model. The offset also implies that reducing the total metal abundance below that of our standard model ($x_{\text{M}} = 10^{-8}$) can only decrease x_e and x_i by at most a factor of ~ 10 . In this sense our uncertainty in the metal abundance (Section 2.4.1) has only a limited impact on the ionization fraction, assuming $x_{\text{M}} < 10^{-8}$. See also Section 3.3.1 where we consider the case $x_{\text{M}} = 0$.

In the limit of high PAH abundance, electron recombination on PAHs dominates electron recombination with HCO^+ . Low equilibrium abundances of free electrons imply the average charge on PAHs $\langle Z \rangle \rightarrow 0$ (Section 3.1). Then the steady-state solutions to Equations (16) and (17) are, respectively,

$$x_e = \frac{\zeta}{x_{\text{PAH}} n_{\text{H}_2} (\alpha_{\text{PAH},e})_{\langle Z \rangle=0}} \quad (20a)$$

$$x_{\text{HCO}^+} = \frac{\zeta}{x_{\text{PAH}} n_{\text{H}_2} (\alpha_{\text{PAH},\text{HCO}^+})_{\langle Z \rangle=0}} \quad (20b)$$

for high PAHs.

Note that in this limit of high PAH abundance, $x_e < x_{\text{HCO}^+}$ because $\alpha_{\text{PAH},e} > \alpha_{\text{PAH},\text{HCO}^+}$; electrons move faster than ions. The remaining negative charge required to maintain charge neutrality is carried by PAHs. That $x_e \neq x_{\text{HCO}^+}$ is relevant for the computation of Am and Re (Section 3.3) because Am depends on x_{HCO^+} (ions carry the bulk of the momentum in a plasma) while Re depends on x_e (electrons are the most mobile charge carriers). Expressions (20a) and (20b) are plotted as diagonal dashed lines in Figure 7; they compare well with the full numerical results, shown as solid lines, in the limit of high x_{PAH} .

The critical PAH abundance dividing these limits is

estimated by equating Equations (20a) to (18):

$$x_{\text{PAH}}^* = \sqrt{\frac{\zeta \alpha_{\text{HCO}^+,e}}{n_{\text{H}_2} (\alpha_{\text{PAH},e})^2}_{(Z)=0}} \quad (21)$$

$$\sim 5 \times 10^{-10} \left(\frac{L_X}{10^{29} \text{ erg s}^{-1}} \right)^{1/2}$$

$$\times \left(\frac{\Sigma}{0.3 \text{ g cm}^{-2}} \right)^{-1/2} \left(\frac{a}{3 \text{ AU}} \right)^{-0.2}$$

for standard metals.

The critical value x_{PAH}^* marks the abundance at which PAHs start to reduce significantly the number of free charges, i.e., the abundance at which electron recombination on PAHs becomes competitive with electron recombination with molecular ions. It is plotted in Figure 7 as a vertical line and does reasonably well at delineating the regime where the ionization fraction does not depend on PAHs from the regime where it does. Note that possible PAH abundances as inferred from observations (Section 2.4.3) happen to straddle x_{PAH}^* .

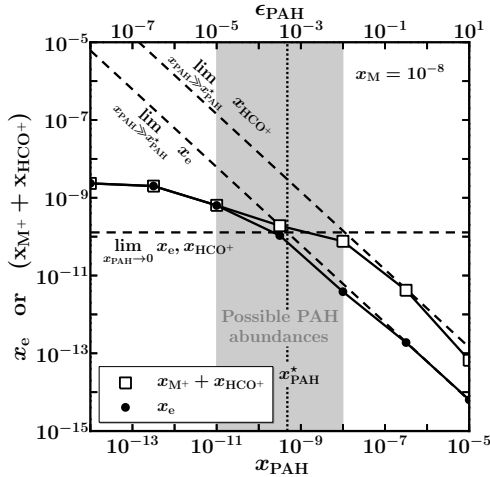


FIG. 7.— Ionization fraction as a function of PAH abundance for $x_{\text{M}} = 10^{-8}$ (standard metal abundance), $a = 3 \text{ AU}$, and $\Sigma = 0.3 \text{ g cm}^{-2}$. Dashed lines: asymptotic values for x_e and x_{HCO^+} of the simplified model of Section 3.2.1. Solid lines: simulation results for fractional electron abundance x_e (solid circles) and fractional ion abundance $x_{\text{M}^+} + x_{\text{HCO}^+}$ (open squares). The dotted vertical line marks x_{PAH}^* (Equation 21), which roughly divides the regime of “low PAH abundance” where electron and ion densities are equal and insensitive to PAH abundance, from the regime of “high PAH abundance” where the ion density exceeds that of electrons and both decrease approximately as $1/x_{\text{PAH}}$. The behavior at high PAH abundance is independent of the metal abundance; compare with Figure 8. The shaded region marks observationally inferred PAH abundances and happens to span the transition from low to high PAH regimes. Simulation data use $\epsilon_{\text{grain}} = 10^{-3}$ for $\epsilon_{\text{PAH}} \leq 10^{-5}$; $\epsilon_{\text{grain}} = 10^{-2}$ for $\epsilon_{\text{PAH}} = 10^{-3.5}$; and $\epsilon_{\text{grain}} = 10^{-1}$ for $\epsilon_{\text{PAH}} \geq 10^{-2}$.

Metal-rich case. — Analogous results are obtained for the metal-rich case as shown in Figure 8, with the only difference that M^+ replaces HCO^+ as the dominant ion. In the limit of low PAH abundance, the abundance of free

charges is

$$x_e = x_{\text{M}^+} = \sqrt{\zeta/n_{\text{H}_2} \alpha_{\text{M}^+,e}} \quad (22)$$

$$\sim 3 \times 10^{-8} \left(\frac{L_X}{10^{29} \text{ erg s}^{-1}} \right)^{1/2}$$

$$\times \left(\frac{\Sigma}{0.3 \text{ g cm}^{-2}} \right)^{-1/2} \left(\frac{a}{3 \text{ AU}} \right)^{-0.5} \quad (23)$$

for high metals and low PAHs.

In going from Equations (22) to (23) we account for the distance dependence of temperature but assume material is optically thin to stellar X-rays. Just as assuming all ions took the form of HCO^+ in the standard model gave a lower limit (Equation 18) for the ionization fraction, assuming that all ions take the form of metals gives an upper limit (Equation 22) because fast recombination of electrons with HCO^+ is neglected.

The analogous asymptotic solutions in the high PAH limit are practically unchanged from Equations (20a) and (20b) because the charging rates of PAHs by HCO^+ and M^+ are similar; the mass of the HCO^+ molecule and that of a metal ion like Mg^+ are similar. The critical PAH abundance at which PAHs begin to reduce the number of free charges is

$$x_{\text{PAH}}^* = \sqrt{\frac{\zeta \alpha_{\text{M}^+,e}}{n_{\text{H}_2} (\alpha_{\text{PAH},e})^2}_{(Z)=0}} \quad (24)$$

$$\sim 2 \times 10^{-12} \left(\frac{L_X}{10^{29} \text{ erg s}^{-1}} \right)^{1/2}$$

$$\times \left(\frac{\Sigma}{0.3 \text{ g cm}^{-2}} \right)^{-1/2} \left(\frac{a}{3 \text{ AU}} \right)^{-0.2}$$

for high metals

and is confirmed by the code.

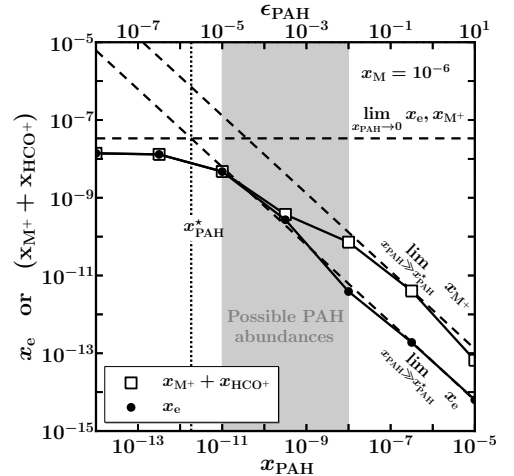


FIG. 8.— Same as Figure 7 but for the metal-rich case ($x_{\text{M}} = 10^{-6}$). The curves for x_e and x_i at high PAH abundance ($x_{\text{PAH}} > x_{\text{PAH}}^*$, where x_{PAH}^* is now given by Equation 24) are essentially the same as in Figure 7: when PAHs dominate charge balance, the metal abundance ceases to matter.

3.3. Degree of Magnetic Coupling: Re and Am

We measure the extent of the MRI-active column by means of the magnetic Reynolds number Re (Equation 1) and the ion-neutral collisional frequency Am (Equation 2). Figures 9 and 10 show both dimensionless numbers as a function of the surface density $\Sigma = N\mu$ penetrated by X-rays at $a = 3$ and 30 AU, respectively, over the range of observationally inferred PAH abundances. We overplot for comparison the solution obtained when we omit PAHs completely.

In both Figures 9 and 10, the middle panels display results for our standard model parameters: $x_M = 10^{-8}$ per H_2 , $L_X = 10^{29}$ erg s $^{-1}$, and $\zeta_{CR} = 0$. In each of the panels on the left and on the right, we vary one of these parameters. We describe here results for our standard model and compare with other test cases in Section 3.3.1.

The middle top panels of Figures 9 and 10 show that if Re were the only discriminant, MRI-active surface layers could well exist, even with PAHs present. At surface densities $\Sigma \sim 0.3$ g cm $^{-2}$ (column densities $N \sim 10^{23}$ cm $^{-2}$), Re lies comfortably above the critical values of 10^2 – 10^4 (Section 1.2) required for plasma to couple to the magnetic field, for a wide range of possible PAH abundances. If the critical $Re \sim 10^2$ (as assumed by BG), and if PAHs are at their lowest possible abundance as inferred from observation ($\epsilon_{PAH} = 10^{-5}$ relative to the ISM; inverted triangles), then the MRI-active layer could extend as far as $\Sigma \sim 20$ g cm $^{-2}$ —if ohmic dissipation were the only limiting factor for the MRI.

But ohmic dissipation is not the only factor. The same margin of safety enjoyed by Re does not at all apply to the ambipolar diffusion number Am , for any surface density. Even in the unrealistic case that there are no PAHs, Am stays < 10 in the middle bottom panels of Figures 9 and 10. By comparison, values of Am exceeding 10^2 are reported by Hawley & Stone (1998) as necessary for the MRI to excite turbulence in predominantly neutral gas. When PAHs are present, Am barely exceeds 1, and then only for the low end of possible PAH abundances. Compared with ohmic dissipation, ambipolar diffusion seems the much greater concern for the viability of the MRI in disk surface layers.

Values of $Am(\Sigma)$ and $Re(\Sigma)$ vary only slightly as the stellocentric distance increases from $a = 3$ AU (Figure 9, middle) to 30 AU (Figure 10, middle); the former decreases while the latter increases, each typically by factors of a few. This behavior is readily understood. First recognize that $x_i \propto a^{-0.6}$ approximately; this is an average scaling between the low PAH limit, which implies $x_i \propto a^{-0.5}$ according to Equation (18), and the high PAH limit, which implies $x_i \propto a^{-5/7} \approx a^{-0.7}$ according to Equation (20b). Combining this result with $n_{H_2} \propto h^{-1} \propto \Omega/T^{1/2} \propto a^{-9/7}$, we find that $Am = x_i n_{H_2} / \Omega \propto a^{-0.4}$. Similarly, $Re = c_s h / D \propto x_e T^{1/2} / \Omega \propto a^{0.7}$.

In computing Am , we have omitted the contribution from collisions between neutral H_2 and negatively charged PAHs. The latter are as well coupled to magnetic fields as molecular ions are—see, e.g., the ion and grain Hall parameters calculated in Section 2.2 of BG. Thus, collisions between H_2 and charged PAHs should increase Am . However, we find that in practice the gain is negligible. We estimate that the collisional rate co-

efficient β_{in} that enters into Am is about the same for charged PAHs as for ions; in both cases a collision with an H_2 molecule is mediated by the induced dipole in H_2 , and the relative velocity is dominated by the thermal speed of H_2 . At $\Sigma \gtrsim 10$ g cm $^{-2}$, charged PAHs are about as abundant as ions and thus raise Am by a factor of 2—but at these Σ 's, Am is already too low for the MRI to be viable. At $\Sigma \lesssim 10$ g cm $^{-2}$ —i.e., at those columns where Am peaks—charged PAHs are much less abundant than ions and thus hardly affect Am .

3.3.1. Higher L_X and T_X , Higher and Lower x_M , and Cosmic-ray Ionization

In each of the leftmost and rightmost panels of Figures 9 and 10, we vary one model parameter away from its standard value. We begin with the case of higher L_X . Increasing L_X certainly raises Re and Am , but as the left panels of Figure 9 show, even a fairly high $L_X = 10^{31}$ erg s $^{-1}$ only causes Am to just exceed 10 at the lowest PAH abundance. In the limit of low PAH abundance, $x_e = x_i \propto L_X^{1/2}$, as predicted by Equation (18). In the limit of high PAH abundance, x_e and x_i scale linearly with L_X , according to Equations (20a) and (20b). Thus the space of possible values of Re and Am narrows with increasing L_X , as the lower envelope increases as L_X while the upper envelope increases as $L_X^{1/2}$.

These same scaling relations, with L_X replaced by the ionization rate ζ at fixed distance, enable us to estimate the effects of a higher T_X , a case we did not explicitly compute using our numerical model. According to IG, raising kT_X from 3 keV (our standard value) to 8 keV increases the ionization rate ζ by factors of 2–4 at $\Sigma = 1$ – 30 g cm $^{-2}$. Thus in the extreme case that $L_X = 10^{31}$ erg s $^{-1}$ and $kT_X = 8$ keV—parameters appropriate only for a small minority of young stars (Telleschi et al. 2007; Preibisch et al. 2005)—we apply the low-PAH scaling relation $x_i \propto \zeta^{1/2}$ to the bottom left panel of Figure 9 to find that the largest possible value of Am is ~ 20 , obtained if PAHs are at their lowest plausible abundance.

The rightmost panels of Figure 9 display the case of a higher metal abundance $x_M = 10^{-6}$ per H_2 . As discussed in Section 2.4.1, the higher metal abundance is not especially realistic and is considered primarily as an exercise. Comparing the middle and right panels of Figure 9, we see that increasing the metal abundance by a factor of 100 raises Re and Am at low PAH abundance by a factor of ~ 10 . At high PAH abundance, Re and Am also increase with increasing metal abundance, but the gain is less. This same behavior is reflected in the solid curves of Figures 7 and 8: at low PAH abundance, increasing x_M by a factor of 100 leads to a factor of ~ 10 increase in $x_e = x_i$, but at high PAH abundance, the now divergent curves for x_e and x_i are essentially independent of metal abundance. Equations (20a) and (20b) from our analytic analysis reflect this insensitivity to metal abundance at high PAH abundance.

At $\Sigma \gtrsim 1$ g cm $^{-2}$, gas temperatures may be so low that all of the metals condense onto grains. The case $x_M = 0$ is shown in the leftmost panels of Figure 10. Here $Am \lesssim 0.1$ for $\Sigma \gtrsim 1$ g cm $^{-2}$, and it seems safe to conclude that X-ray driven MRI is unviable under these conditions.

Additional ionization by “sideways cosmic-rays” at $a =$

30 AU is considered in the rightmost panels of Figure 10. These cosmic-rays, which we have imagined enter the disk edge-on from the outside, dominate stellar X-rays at large Σ . At $\Sigma \sim 10 \text{ g cm}^{-2}$ —comparable to the full surface density of the disk at $a = 30 \text{ AU}$ —sideways cosmic-rays raise the maximum value of Am to ~ 2 . We have verified that the gains in Am afforded by cosmic-rays are consistent with our scalings of x_e and x_i with ζ as derived above.

3.3.2. Chemical Equilibration Timescales vs. Dynamical Timescales

In assessing whether disk surface layers are MRI-active, we have relied on the critical value $Am^* \sim 10^2$ reported by HS. As a simplifying assumption, HS held fixed the global (box-integrated) ion abundance in each of their simulations. A fixed ion abundance would apply if the chemical equilibration timescale t_{eq} exceeds the dynamical timescale $t_{\text{dyn}} = \Omega^{-1}$ over which HS’s simulations ran. A fixed ion abundance would also apply if ion recombination occurs predominantly on condensates, regardless of $t_{\text{eq}}/t_{\text{dyn}}$ (e.g., Mac Low et al. 1995). This last statement follows from our Equation (20b), which shows $x_i n_{\text{H}_2}$ does not depend on n_{H_2} in the high condensate limit.

The high condensate limit applies for PAH abundances near the high end of those inferred from observation (Figure 7). For this high PAH case we expect the assumption of constant ion abundance, and by extension the results of HS, to hold. For high PAH abundance and our standard X-ray luminosity, $Am < 1$ for all Σ and a (Figure 9), and our conclusion that X-ray-driven MRI shuts down everywhere seems safe.

For PAH abundances at the low end of those inferred from observation, Equation (20b) for the high condensate limit does not apply. Moreover, as shown in Figure 11, $t_{\text{eq}}/t_{\text{dyn}} < 1$ —but only by a factor of 10 at most for the low PAH case and for $\Sigma \lesssim 10 \text{ g cm}^{-2}$. Because $t_{\text{eq}}/t_{\text{dyn}} \gtrsim 0.1$ under these conditions, the assumption of constant ion abundance, although not strictly valid, might still be good enough that the results of HS hold to order unity. But even if they do not, we would argue that the sign of any correction for a dynamically variable ion abundance would only hurt the prospects for MRI turbulence. In the simulations of HS—see also Brandenburg & Zweibel (1994) and Mac Low et al. (1995)—ions became concentrated in thin filaments within magnetic nulls. Recombination rates inside the dense filaments were higher than those outside. Were such simulations to account for ion recombination, lower ion densities within the filaments would result, and neutrals would be even less coupled to ions. Consequently, Am^* would be even higher than the reported value of $\sim 10^2$.

3.4. Comparison with Previous Work: Ionization Fractions

The ionization chemistry in disks remains inherently uncertain, with rate coefficients for many reactions in the UMIST database determined to no better than factors of ~ 3 (Vasyunin et al. 2008). A measure of the uncertainty in the ionization fraction in disks is given by

the differences between the simple and complex networks computed by BG, which amount to factors of 2–10 for the electron fraction x_e . We should reproduce their results by at least this margin, as a validation of our code. In the following we directly compare our results to those of BG and TCS, adjusting the input parameters of our code to match theirs. Once we match these input parameters, any difference in our codes’ outputs should result primarily from our different chemical networks (ours is the simplest of the three), and not from differences in radiative transfer, as all our codes rely on the ionization rates calculated by Igea & Glassgold (1999).

We start with BG by computing x_e as a function of density n_{H_2} at a fixed ionization rate $\zeta = 10^{-17} \text{ s}^{-1}$, following their Figure 3. We reset $T = 280 \text{ K}$, $x_{\text{M}} = 2.5 \times 10^{-8}$ per H_2 , and the electron-grain sticking coefficient $S_e = 0.03$ to match their standard parameters. To compare to their “grain-free” case, we run our code without any PAHs or grains. To compare to their standard monodispersion of grains, we run our code with a single population of grains having $s = 0.1 \mu\text{m}$, internal density $\rho_s = 3 \text{ g cm}^{-3}$, and a mass fraction of 1% relative to gas. Figure 12 shows the comparison. Our results for the condensate-free case track those of BG, but are higher by factors of 3–10 depending on whether the comparison is made with their simple or complex network. For the case with grains, the agreement with the simple model is excellent and that with the complex model is good to a factor of 2.

In Figure 13, we make a similar comparison with TCS, computing x_e as a function of N at a distance of $a = 5 \text{ AU}$ from an X-ray source of $L_{\text{X}} = 2 \times 10^{30} \text{ erg s}^{-1}$ and $kT_{\text{X}} = 5 \text{ keV}$, for $T = 125 \text{ K}$ and a metal abundance of $x_{\text{M}} = 6.8 \times 10^{-7}$ per H_2 . We consider the two cases of their Figure 1, one without any grains or PAHs, and another with a single population of grains having $s = 1 \mu\text{m}$, $\rho_s = 5 \text{ g cm}^{-3}$, and a mass fraction of 1%. For both cases our computed electron abundances are higher, but only by factors of 2 or less.

These comparisons with BG and TCS give us confidence that we have computed ionization fractions about as well as they did. Where our ionization fractions differ, ours are often higher. Our higher values will only bolster the conclusion we make in Section 4 that thicknesses of X-ray-ionized MRI-active surface layers have been overestimated by them and others.

4. SUMMARY AND DISCUSSION

In Section 1, we presented the evidence that holes and gaps of transitional disks are cleared by companions to their host stars. Residing within the hole, these companions could either be stars—already observed in about half of all transitional systems—or multi-planet systems. A single Jupiter-mass planet on a circular orbit carves out too narrow a gap to explain the large cavities inferred from observations. But multiple planets can shuttle gas quickly from one planet to the next, all the way down to the central star. Surface densities fall in inverse proportion to radial infall speeds, and radial infall speeds can approach freefall speeds for sufficiently many and massive planets. In this way, multi-planet systems might help to clear holes and simultaneously sustain stellar accretion rates that approach those in disks without holes. The more eccentric the planets’ orbits, the fewer of them

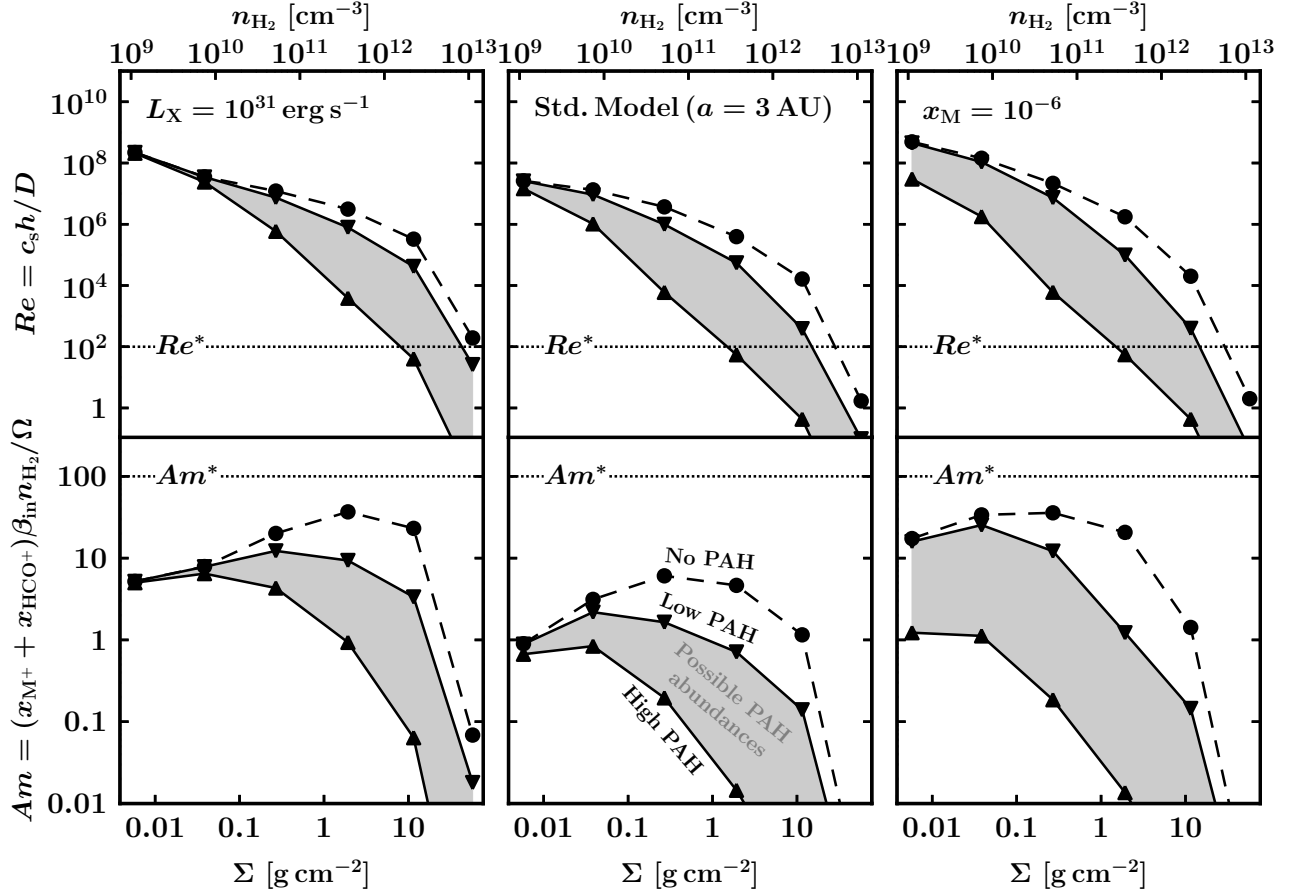


FIG. 9.— Magnetic Reynolds number Re and ambipolar diffusion number Am as a function of surface density Σ at $a = 3$ AU. The middle panels show results for our standard model ($x_M = 10^{-8}$, $L_X = 10^{29}$ erg s $^{-1}$, $\zeta_{CR} = 0$). The side panels have the same parameters as our standard model, except for a $100\times$ more luminous X-ray source (left panels), and a $100\times$ greater metal abundance (right panels). Oppositely pointing triangles bracket values for Am and Re corresponding to possible PAH abundances. These abundances were inferred in Section 2.4.3 from observations. The dashed curve refers to the case with no PAHs and is shown for comparison only. Polycyclic aromatic hydrocarbons reduce ionization fractions and thus the degree of magnetic coupling by an order of magnitude or more. The dotted lines mark the critical values Am^* and Re^* above which coupling between magnetic fields and neutral gas is sufficient to drive the MRI (Section 1.2). The curves for Am first rise as Σ increases—a consequence of the increasing number density—and then fall as the ion fraction decreases, never reaching Am^* . Ambipolar diffusion threatens the MRI more than ohmic dissipation does. If the critical Am required for good collisional coupling between ions and neutrals is $Am^* = 10^2$, as evidenced in simulations by Hawley & Stone (1998), then even a disk without PAHs cannot sustain X-ray-driven MRI at any Σ .

may be required to explain a given hole size. Accretion in the presence of multi-planet systems has not received much attention and seems an interesting area for future simulation (e.g., Zhu et al. 2010, submitted).

Stellar or planetary companions regulate accretion velocities v but do not give rise to mass accretion rates \dot{M} in the first place. A planet orbiting just inside the circumference of a disk hole exerts torques to repel gas in the hole’s rim away from the star. Thus, the shepherding planet may reduce \dot{M} —and indeed accretion rates in transitional systems tend to be smaller than those in conventional disks (Najita et al. 2007)—but the planet does not initiate disk accretion. A separate mechanism must act to pull or diffuse gas inward from the hole rim to supply the stellar accretion rates that are observed. That mechanism may be turbulence driven by the magnetorotational instability (MRI), activated by stellar radiation ionizing rim gas. Whether the MRI can operate depends on how well ionized the gas is. The greater the free electron fraction, the greater the magnetic Reynolds number Re , and the less ohmic dissipation dampens the MRI. The greater the atomic and molecular ion densities, the greater the collisional rate Am between neutral particles and ions, and the less ambipolar diffusion weakens the MRI.

A principal threat to the MRI is posed by dust grains, which adsorb electrons and ions. The smallest grains may present the biggest danger, because in many particle size distributions the smallest grains have the greatest surface area for attachment. The smallest grains that can also be detected observationally are polycyclic aromatic hydrocarbons (PAHs), each several angstroms across and containing of order a hundred carbon atoms. These macromolecules may reside in the very disk surface layers that promise to be MRI-active. Excited by soft ultraviolet radiation, PAHs fluoresce in a distinctive set of infrared emission lines detectable from *Spitzer* and from the ground. The hydrocarbon molecules are probably generated locally, photo-sputtered off larger particles exposed to hard UV and X-ray radiation from host stars.

To assess the impact of PAHs on the MRI, we need to know PAH abundances relative to gas. These can be inferred from observed PAH emission lines. Unfortunately such inferences are model dependent; they depend on knowing the local grain opacity, because the soft UV radiation that excites PAHs is also absorbed by grains. In other words, observed PAH line intensities depend on PAH-to-dust ratios. It follows that the quantity of interest to us—the PAH-to-gas ratio—depends on knowing the dust-to-gas ratio. The latter can vary widely with the degree to which grains settle toward disk midplanes. The more grains have settled, the lower are local dust-to-gas ratios, and the lower the PAH-to-gas abundance that is needed to explain a given set of PAH emission spectra. By compiling a few lines of model-dependent evidence from the literature, we estimated that disk PAHs have abundances anywhere from 10^{-11} – 10^{-8} per H_2 , with lower values corresponding to a greater degree of dust settling.

Such PAH abundances, although depleted relative to the ISM by 10^{-5} – 10^{-2} , are still large enough to significantly weaken the MRI in disk surface layers. In fact, they might even shut off X-ray-driven MRI altogether,

everywhere. For stellar X-ray luminosities of $L_X = 10^{29}$ – 10^{31} erg s $^{-1}$ and X-ray stopping columns of $\Sigma \sim 1$ – 10 g cm $^{-2}$, PAHs reduce electron and ion densities—which are not equal when PAHs are present—by factors of ~ 10 or more. At these surface densities, the collisional coupling frequency $Am \approx 10^{-3}$ – 10 , depending on PAH abundance and X-ray luminosity. These values fall short, by 1–5 orders of magnitude, of the critical value $Am^* \sim 10^2$ required for good coupling between ions and neutrals, as measured in simulations by Hawley & Stone (1998, HS). The potentially catastrophic effect that small grains can have on the MRI was highlighted by Bai & Goodman (2009, BG). Our study grounds their concern in real-life observations.

Other studies reported X-ray-driven MRI-active surface layers to be alive and well (e.g., Chiang & Murray-Clay 2007, CMC; Turner, Carballido, & Sano 2010, TCS; and BG, in many of whose models the active layer extended to ~ 1 g cm $^{-2}$, even with grains present). We should understand why our conclusions differ from theirs. In part, the difference arises because previous studies neglected PAHs. A further difference with TCS is that they assumed a metal abundance of $x_M = 6.8 \times 10^{-7}$ per H_2 , nearly 2 orders of magnitude higher than our standard model value, and one that we find difficult to justify. Still another difference, as significant as any of the ones just mentioned, is the criterion used for whether ambipolar diffusion defeats the MRI. Turner et al. (2010) assumed $Am^* \sim 1$ (see their Equation 9). Bai & Goodman (2009) did not present results for Am . Using their data, we computed the Am values characterizing their claimed active layers. At $a \gtrsim 1$ AU, the Am values of BG’s grain-free active layer are at most on the order of unity. For BG’s standard models containing grains, $Am \approx 0.0004$ – 0.4 , with the lowest value corresponding to $a = 50$ AU and a population of grains having two sizes, and the highest value corresponding to $a = 1$ AU and a single-sized grain population (we computed both limits using results from their complex chemical network). Hawley & Stone (1998) showed that when $Am \lesssim 0.01$, ions and neutrals were effectively decoupled. Even when $Am \sim 1$, HS showed that the MRI saturation amplitude scaled with the ion and not the neutral density, with the neutrals acting to damp out MRI turbulence in the ions. If the MRI drives turbulence only in the ions of protoplanetary disks, it might as well not operate at all, given how overwhelmingly neutral such disks are.

4.1. Future Directions

We have shown in this paper that the MRI cannot drive surface layer accretion under typical circumstances in protoplanetary disks, either transitional or conventional, if the critical $Am^* \sim 10^2$ and if stellar X-rays and Galactic cosmic-rays are the dominant source of ionization. These two “if”s are subject to further investigation. We discuss each in turn.

We are not aware of more modern estimates of Am^* apart from that given by HS. As these authors cautioned, numerical resolution is a greater concern for two-fluid simulations than for single-fluid ones, and HS did not demonstrate convergence of their results with resolution. In addition, the value of Am^* was not as precisely determined by HS for toroidal field geometries as for vertical ones—although $Am^* \sim 10^2$ did seem to apply equally

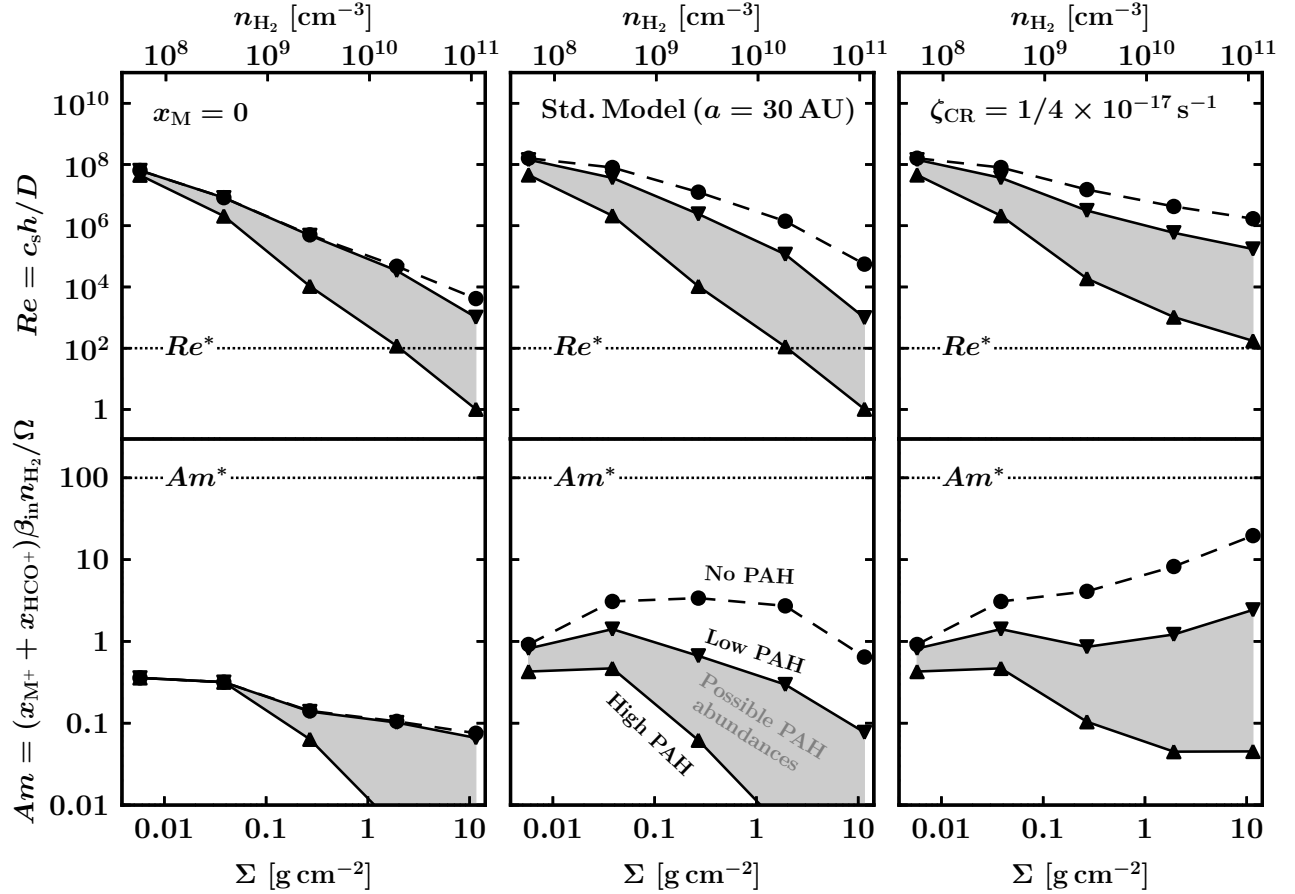


FIG. 10.— Same as Figure 9, but at a stellocentric distance of $a = 30$ AU. The middle panels show results for our standard model ($x_M = 10^{-8}$, $L_X = 10^{29}$ erg s^{-1} , $\zeta_{CR} = 0$). The side panels have the same parameters as our standard model, except that gas-phase metals are omitted in the left panels ($x_M = 0$), and sideways cosmic-rays are added in the right panels ($\zeta_{CR} = 1/4 \times 10^{-17}$ s $^{-1}$).

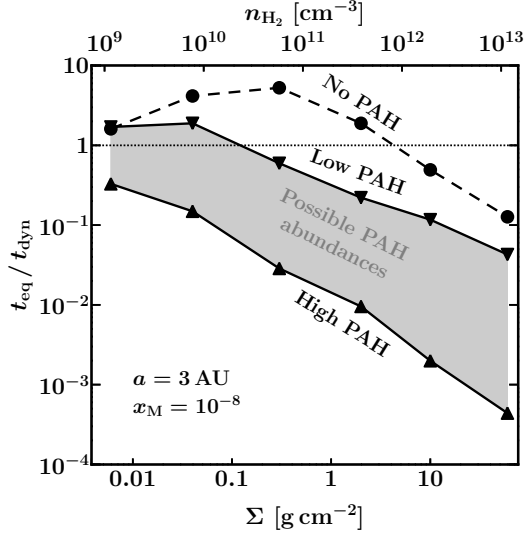


FIG. 11.— Ratio of the chemical equilibration timescale t_{eq} , computed according to the procedure described in Section 2.6, to the dynamical time $t_{\text{dyn}} = \Omega^{-1}$, for $a = 3$ AU and $x_{\text{M}} = 10^{-8}$. Values of $t_{\text{eq}}/t_{\text{dyn}}$ at $a = 30$ AU are typically lower than those shown here by factors of 3 or less. Simulations by HS assumed a constant (volume-integrated) abundance of ions, a condition satisfied if $t_{\text{eq}}/t_{\text{dyn}} > 1$. The ion abundance is also constant if ion recombination occurs primarily on condensates (see Equation 20b), a situation that obtains for PAH abundances near the high end of those inferred from observations. For the lowest possible PAH abundances, $0.1 < t_{\text{eq}}/t_{\text{dyn}} < 1$ at $\Sigma = 0.1$ – 10 g cm^{-2} . In this low PAH case, the results of HS might still be expected to apply to order unity. Even if they do not, we argue in the main text that when $t_{\text{eq}}/t_{\text{dyn}} < 1$ the effects of ambipolar diffusion should be even stronger than reported by HS.

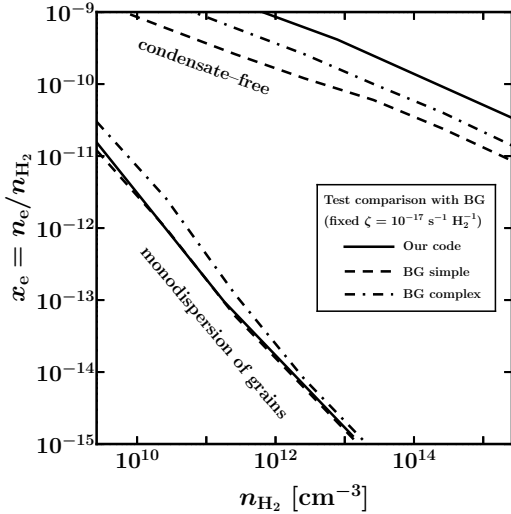


FIG. 12.— Test comparison with BG: electron abundance as a function of gas density at a fixed ionization rate of $\zeta = 10^{-17} \text{ s}^{-1} \text{ H}_2^{-1}$. The upper set of lines are for a condensate-free system, and the lower set are for a monodispersion of grains. Results from BG were drawn from their Figure 3. To generate our results, the parameters of our code were reset to those of BG: temperature $T = 280$ K, metal abundance $x_{\text{M}} = 2.5 \times 10^{-8}$ per H_2 , electron-grain sticking coefficient $S_{\text{e}} = 0.03$, grain radius $s = 0.1 \mu\text{m}$, internal grain density $\rho_{\text{s}} = 3 \text{ g cm}^{-3}$, and a mass fraction in grains relative to gas of 1%.

well to the cases of uniform vertical field and zero net

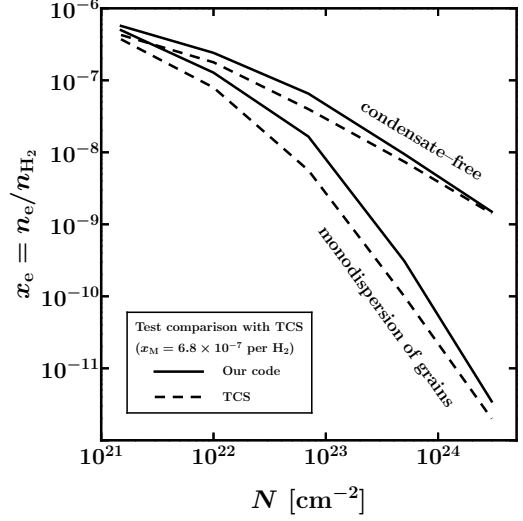


FIG. 13.— Test comparison with TCS: electron abundance as a function of column depth penetrated by X-rays. The upper pair of lines are for a condensate-free system, and the lower pair are for a monodispersion of grains. Ionization rates are from IG. Results from TCS are taken from their Figure 1. To generate our results, we reset the parameters of our code to match those of TCS: stellocentric distance $a = 5$ AU, X-ray luminosity $L_{\text{X}} = 2 \times 10^{30} \text{ erg s}^{-1}$, temperature $T = 125$ K, metal (magnesium) abundance $x_{\text{M}} = 6.8 \times 10^{-7}$ per H_2 , electron-grain sticking coefficient $S_{\text{e}} = 0.03$, grain radius $s = 1 \mu\text{m}$, internal grain density $\rho_{\text{s}} = 5 \text{ g cm}^{-3}$, and a mass fraction in grains relative to gas of 1%.

vertical field. Perhaps higher resolution simulations will reveal that $Am^* < 10^2$ —although accounting for ion recombination in these simulations should only increase Am^* (Section 3.3.2).

The second possibility is that our model has neglected a significant source of ionization. Stellar radiation just longward of the Lyman limit—so-called far ultraviolet (FUV) radiation at photon energies between ~ 6 and 13.6 eV—can ionize trace species such as C, S, Mg, Si, and Al (e.g., Cruddace et al. 1974). Of these elements, C and S may be the most important, as they are the most abundant and possibly least depleted onto grains. For example, if the full solar abundance of C were singly ionized, the ion fraction x_{i} would be a few $\times 10^{-4}$, or 5 orders of magnitude higher than the largest values of x_{i} reported in this paper! At disk midplanes which are shielded from photodissociating radiation, an order-unity fraction of the full solar abundance of C is expected to take the form of CO ($x_{\text{CO}} = 10^{-4}$; Aikawa et al. 1996). As computed in chemical models by Gorti & Hollenbach (2004; see also Tielens & Hollenbach 1985 and Kaufman et al. 1999), CO near disk surfaces photodissociates nearly entirely by FUV radiation into a layer of neutral C. At the highest altitudes, nearly all of this carbon is photoionized by FUV radiation. The column density of C^+ depends on how many small grains having sizes $\lesssim 0.1 \mu\text{m}$ are present, as grains compete to absorb the same FUV photons that photodissociate CO and photoionize C.

We may estimate maximum FUV-ionized column densities by neglecting such dust extinction, and by neglecting shielding of FUV radiation by molecular hydrogen. Consider a trace species T whose total number density regardless of ionization state is $f_{\text{T}}n_{\text{H}_2}$. Take all of T to be singly ionized within a Strömgen slab at the disk sur-

face: $n_{T^+} = n_e = f_T n_{H_2}$. Per unit surface area of slab, the rate of photoionizations balances the rate of radiative recombinations:

$$\begin{aligned} \frac{L_{FUV}}{E_{FUV} 4\pi a^2} &\sim n_{T^+} n_e \alpha_{T^+,e} h \\ &\sim f_T^2 n_{H_2}^2 \alpha_{T^+,e} h, \end{aligned} \quad (25)$$

where the FUV luminosity capable of ionizing T is $L_{FUV} \sim 10^{30}$ erg s⁻¹ (Gorti et al. 2009), the photon energy $E_{FUV} \sim 10$ eV, the rate coefficient $\alpha_{T^+,e} \sim 4 \times 10^{-12}$ cm³ s⁻¹ at an FUV-heated gas temperature of 300 K, and the slab thickness $h \sim 0.1a$. Solve for the hydrogen column

$$\begin{aligned} N_{FUV} &= n_{H_2} h \\ &\sim 2 \times 10^{22} \left(\frac{L_{FUV}}{10^{30} \text{ erg s}^{-1}} \right)^{1/2} \\ &\quad \times \left(\frac{3 \text{ AU}}{a} \right)^{1/2} \left(\frac{10^{-4}}{f_T} \right) \text{ cm}^{-2}, \end{aligned} \quad (26)$$

or equivalently

$$\begin{aligned} \Sigma_{FUV} &= N_{FUV} \mu \\ &\sim 0.07 \left(\frac{L_{FUV}}{10^{30} \text{ erg s}^{-1}} \right)^{1/2} \\ &\quad \times \left(\frac{3 \text{ AU}}{a} \right)^{1/2} \left(\frac{10^{-4}}{f_T} \right) \text{ g cm}^{-2}. \end{aligned} \quad (27)$$

In Equation (27), we have normalized f_T to its highest plausible value, appropriate for C. An MRI-active surface density $\Sigma_{FUV} \sim 0.07$ g cm⁻² is modest, and would drive mass accretion rates only barely observable. Lowering f_T would increase Σ_{FUV} . But accounting for extinction of FUV radiation by dust and molecular hydrogen would decrease Σ_{FUV} . We are currently undertaking a more careful study of FUV ionization to quantify these effects.

Neal Turner provided invaluable feedback during formative stages of this work. We thank Xue-Ning Bai, Kees Dullemond, Josh Eisner, Vincent Geers, Al Glassgold, Uma Gorti, Lee Hartmann, David Hollenbach, Anders Johansen, Yoram Lithwick, Dimitri Semenov, Greg Sloan, Jim Stone, Marten van Kerkwijk, Yanqin Wu, and Andrew Youdin for discussions. Xue-Ning Bai and Jim Stone provided encouraging feedback that led to additional analyses such as that in section 3.3.2. Zhao-huan Zhu and Lee Hartmann generously shared their preprint which impressed upon us the need for grain growth to explain the low optical depths of transitional disk holes. An anonymous referee provided a thoughtful and thorough report that alerted us to the possibility of “sideways cosmic-rays,” and that motivated us to consider the effects of UV ionization. We also thank our editor, Eric Feigelson, for additional comments on our manuscript. E.C. acknowledges the hospitality of the Kavli Institute for Astronomy and Astrophysics in Beijing, China, where a portion of this work was carried out. This work was funded by the National Science Foundation, in part through a Graduate Research Fellowship awarded to D.P.-B.

REFERENCES

- Aikawa, Y., Miyama, S. M., Nakano, T., & Umebayashi, T. 1996, *ApJ*, 467, 684
- Allamandola, L. J., Hudgins, D. M., & Sandford, S. A. 1999, *ApJ*, 511, L115
- Allamandola, L. J., Tielens, A. G. G. M., & Barker, J. R. 1989, *ApJS*, 71, 733
- Artymowicz, P., & Lubow, S. H. 1994, *ApJ*, 421, 651
- . 1996, *ApJ*, 467, L77+
- Bai, X., & Goodman, J. 2009, *ApJ*, 701, 737
- Balbus, S. A. 2009, to be published in “Physical processes in circumstellar disks around young stars” (Chicago, IL: University of Chicago Press)
- Blum, J., & Wurm, G. 2008, *ARA&A*, 46, 21
- Borucki, W. J., & Whitten, R. C. 2008, *Planet. Space Sci.*, 56, 19
- Brandenburg, A., & Zweibel, E. G. 1994, *ApJ*, 427, L91
- Brown, J. M., Blake, G. A., Qi, C., Dullemond, C. P., Wilner, D. J., & Williams, J. P. 2009, *ApJ*, 704, 496
- Burns, J. A., Lamy, P. L., & Soter, S. 1979, *Icarus*, 40, 1
- Calvet, N., D’Alessio, P., Hartmann, L., Wilner, D., Walsh, A., & Sitko, M. 2002, *ApJ*, 568, 1008
- Calvet, N., et al. 2005, *ApJ*, 630, L185
- Caselli, P., Walmsley, C. M., Terzieva, R., & Herbst, E. 1998, *ApJ*, 499, 234
- Chiang, E., & Murray-Clay, R. 2007, *Nature Physics*, 3, 604
- Chiang, E., & Youdin, A. N. 2010, *Annu. Rev. Earth Planet. Sci.*, 38, 493
- Chiang, E. I., & Goldreich, P. 1997, *ApJ*, 490, 368
- Chiang, E. I., Joungh, M. K., Creech-Eakman, M. J., Qi, C., Kessler, J. E., Blake, G. A., & van Dishoeck, E. F. 2001, *ApJ*, 547, 1077
- Crida, A., & Morbidelli, A. 2007, *MNRAS*, 377, 1324
- Crudace, R., Paresce, F., Bowyer, S., & Lampton, M. 1974, *ApJ*, 187, 497
- D’Alessio, P., Calvet, N., Hartmann, L., Franco-Hernández, R., & Servín, H. 2006, *ApJ*, 638, 314
- D’Alessio, P., Calvet, N., Hartmann, L., Lizano, S., & Cantó, J. 1999, *ApJ*, 527, 893
- D’Alessio, P., et al. 2005, *ApJ*, 621, 461
- Draine, B. T., Roberge, W. G., & Dalgarno, A. 1983, *ApJ*, 264, 485
- Draine, B. T., & Sutin, B. 1987, *ApJ*, 320, 803
- Dullemond, C. P., & Dominik, C. 2004, *A&A*, 421, 1075
- Dullemond, C. P., Dominik, C., & Natta, A. 2001, *ApJ*, 560, 957
- Dullemond, C. P., Henning, T., Visser, R., Geers, V. C., van Dishoeck, E. F., & Pontoppidan, K. M. 2007, *A&A*, 473, 457
- Eisner, J. A., Monnier, J. D., Tuthill, P., & Lacour, S. 2009, *ApJ*, 698, L169
- Espaillet, C., Calvet, N., D’Alessio, P., Hernández, J., Qi, C., Hartmann, L., Furlan, E., & Watson, D. M. 2007a, *ApJ*, 670, L135
- Espaillet, C., et al. 2007b, *ApJ*, 664, L111
- Fleming, T. P., Stone, J. M., & Hawley, J. F. 2000, *ApJ*, 530, 464
- Fromang, S., Terquem, C., & Balbus, S. A. 2002, *MNRAS*, 329, 18
- Gammie, C. F. 1996, *ApJ*, 457, 355
- Geers, V. C., van Dishoeck, E. F., Visser, R., Pontoppidan, K. M., Augereau, J., Habart, E., & Lagrange, A. M. 2007, *A&A*, 476, 279
- Geers, V. C., et al. 2006, *A&A*, 459, 545
- Getman, K. V., Feigelson, E. D., Broos, P. S., Micela, G., & Garmire, G. P. 2008a, *ApJ*, 688, 418
- Getman, K. V., Feigelson, E. D., Micela, G., Jardine, M. M., Gregory, S. G., & Garmire, G. P. 2008b, *ApJ*, 688, 437
- Glassgold, A. E., Najita, J., & Igea, J. 1997, *ApJ*, 480, 344
- . 2004, *ApJ*, 615, 972
- Goldreich, P., & Tremaine, S. 1980, *ApJ*, 241, 425
- Gorti, U., Dullemond, C. P., & Hollenbach, D. 2009, *ApJ*, 705, 1237

- Gorti, U., & Hollenbach, D. 2004, *ApJ*, 613, 424
 Goto, M., et al. 2009, *ApJ*, 693, 610
 Habart, E., Natta, A., & Krügel, E. 2004, *A&A*, 427, 179
 Hawley, J. F., & Stone, J. M. 1998, *ApJ*, 501, 758
 Hughes, A. M., Wilner, D. J., Calvet, N., D'Alessio, P., Claussen, M. J., & Hogerheijde, M. R. 2007, *ApJ*, 664, 536
 Igea, J., & Glassgold, A. E. 1999, *ApJ*, 518, 848
 Ilgner, M., & Nelson, R. P. 2006, *A&A*, 445, 205
 Ireland, M. J., & Kraus, A. L. 2008, *ApJ*, 678, L59
 Jackson, J. D. 1975, *Classical Electrodynamics* (New York: Wiley)
 Jenkins, E. B. 2009, *ApJ*, 700, 1299
 Jensen, E. J., & Thomas, G. E. 1991, *J. Geophys. Res.*, 96, 18603
 Kaufman, M. J., Wolfire, M. G., Hollenbach, D. J., & Luhman, M. L. 1999, *ApJ*, 527, 795
 Keller, L. D., et al. 2008, *ApJ*, 684, 411
 Kim, K. H., et al. 2009, *ApJ*, 700, 1017
 Li, A., & Draine, B. T. 2001, *ApJ*, 554, 778
 Lodders, K. 2003, *ApJ*, 591, 1220
 Lubow, S. H., & D'Angelo, G. 2006, *ApJ*, 641, 526
 Lubow, S. H., Seibert, M., & Artymowicz, P. 1999, *ApJ*, 526, 1001
 Mac Low, M., Norman, M. L., Konigl, A., & Wardle, M. 1995, *ApJ*, 442, 726
 Marsh, N., & Svensmark, H. 2003, *J. Geophys. Res. (Atmospheres)*, 108, 4195
 Masset, F., & Snellgrove, M. 2001, *MNRAS*, 320, L55
 McCabe, C., Duchêne, G., & Ghez, A. M. 2003, *ApJ*, 588, L113
 Morbidelli, A., & Crida, A. 2007, *Icarus*, 191, 158
 Najita, J. R., Strom, S. E., & Muzerolle, J. 2007, *MNRAS*, 378, 369
 Natanson, G. L. 1960, *Sov. Physics-Tech. Phys.*, 5, 538
 Natta, A., Testi, L., Calvet, N., Henning, T., Waters, R., & Wilner, D. 2007, in *Protostars and Planets V*, ed. B. Reipurth, D. Jewitt, & K. Keil (Tucson, AZ: Univ. of Arizona Press), 767
 Ochi, Y., Sugimoto, K., & Hanawa, T. 2005, *ApJ*, 623, 922
 Oppenheimer, M., & Dalgarno, A. 1974, *ApJ*, 192, 29
 Paardekooper, S., & Mellema, G. 2006, *A&A*, 453, 1129
 Parthasarathy, R. 1976, *J. Geophys. Res.*, 81, 2392
 Pendleton, Y. J., & Allamandola, L. J. 2002, *ApJS*, 138, 75
 Preibisch, T., et al. 2005, *ApJS*, 160, 401
 Ratzka, T., Leinert, C., Henning, T., Bouwman, J., Dullemond, C. P., & Jaffe, W. 2007, *A&A*, 471, 173
 Rice, W. K. M., Armitage, P. J., Wood, K., & Lodato, G. 2006, *MNRAS*, 373, 1619
 Robertson, S., & Sternovsky, Z. 2008, *Phys. Plasmas*, 15, 040702
 Salyk, C., Blake, G. A., Boogert, A. C. A., & Brown, J. M. 2007, *ApJ*, 655, L105
 Sano, T., & Inutsuka, S. 2001, *ApJ*, 561, L179
 Sano, T., Miyama, S. M., Umebayashi, T., & Nakano, T. 2000, *ApJ*, 543, 486
 Sano, T., & Stone, J. M. 2002, *ApJ*, 570, 314
 Schunk, R. W., & Nagy, A. F. 2004, *Ionospheres* (Cambridge: Cambridge Univ. Press)
 Sloan, G. C., et al. 2005, *ApJ*, 632, 956
 Stelzer, B., & Schmitt, J. H. M. M. 2004, *A&A*, 418, 687
 Strom, S. E., Edwards, S., & Skrutskie, M. F. 1990, in *ASP Conf. Ser. 9, Cool Stars, Stellar Systems, and the Sun*, ed. G. Wallerstein (San Francisco, CA: ASP) 275
 Strom, S. E., Edwards, S., & Skrutskie, M. F. 1993, in *Protostars and Planets III*, ed. E. H. Levy & J. I. Lunine (Tucson AZ: Univ. of Arizona Press) 837
 Telleschi, A., Güdel, M., Briggs, K. R., Audard, M., & Palla, F. 2007, *A&A*, 468, 425
 Tielens, A. G. G. M., & Hollenbach, D. 1985, *ApJ*, 291, 747
 Turner, N. J., Carballido, A., & Sano, T. 2010, *ApJ*, 708, 188
 Turner, N. J., & Drake, J. F. 2009, *ApJ*, 703, 2152
 Turner, N. J., Sano, T., & Dziourkevitch, N. 2007, *ApJ*, 659, 729
 Umebayashi, T., & Nakano, T. 1981, *PASJ*, 33, 617
 Vasyunin, A. I., Semenov, D., Henning, T., Wakelam, V., Herbst, E., & Sobolev, A. M. 2008, *ApJ*, 672, 629
 Visser, R., Geers, V. C., Dullemond, C. P., Augereau, J., Pontoppidan, K. M., & van Dishoeck, E. F. 2007, *A&A*, 466, 229
 Ward, W. R. 2009, in *Lunar and Planetary Institute Science Conference Abstracts, Vol. 40*, (Houston, TX: Lunar and Planetary Institute), 1477
 Watson, A. M., Stapelfeldt, K. R., Wood, K., & Ménard, F. 2007, in *Protostars and Planets V*, ed. B. Reipurth, D. Jewitt, & K. Keil (Tucson, AZ: Univ. of Arizona Press), 523
 Whitten, R. C., Borucki, W. J., & Tripathi, S. 2007, *J. Geophys. Res. (Planets)*, 112, 4001
 Wolk, S. J., Harnden, Jr., F. R., Flaccomio, E., Micela, G., Favata, F., Shang, H., & Feigelson, E. D. 2005, *ApJS*, 160, 423
 Woodall, J., Agúndez, M., Markwick-Kemper, A. J., & Millar, T. J. 2007, *A&A*, 466, 1197
 Wyatt, M. C. 2008, *ARA&A*, 46, 339
 Zhu, Z., Nelson, R. P., Hartmann, L., Espaillat, C., & Calvet, N. 2010, submitted

Note added in proof.— In a private communication, Xue-Ning Bai reports that in new, unstratified MRI simulations, the Shakura-Sunyaev transport parameter α is at most $\sim 10^{-3}$ when $Am \sim 1$. Combining his result with the results of our paper, we estimate that the mass accretion rate in the surface layer of a conventional disk at 3 AU is $\sim 10^{-11} M_{\odot} \text{ yr}^{-1}$. At the rim of a transitional disk, we would predict an accretion rate that is lower by a factor of $\sim h/a$, or $\sim 10^{-12} M_{\odot} \text{ yr}^{-1}$ at 3 AU. These theoretical accretion rates are too low to explain the observed accretion rates of most disks. The situation is similar at 30 AU, where the surface layer accretion rate in conventional (transitional) disks can only be as high as $\sim 10^{-9} (10^{-10}) M_{\odot} \text{ yr}^{-1}$ if Galactic cosmic-rays can penetrate the disk edge-on (see our Figure 10, right).